Modeling of the Liver Deformation During Breathing in Radiation Therapy

by

Hesham Alghodhaifi

A thesis submitted in partial fulfillment
of the requirements for the degree of
Master of Science in Engineering
(Electrical Engineering)
at the University of Michigan -Dearborn
2017

Master's Thesis Committee:

Professor Selim Awad, Co-Chair
Professor James Balter, Co-Chair, University of Michigan
Professor Sridhar Lakshmanan

2017

To my mother and father, who raised me and taught me how to respect, love, care, and think

To my brother, Dr. Naif, who guided me and encouraged me to continue my education

ACKNOWLEDGMENTS

Firstly, I would like to express my sincere gratitude to my advisor, Prof. Selim Awad, for his support, patience, motivation, and immense knowledge. His guidance helped me through all the time of researching and writing this thesis. I would like also to thank my co-advisor, Prof. James Balter. I am not sure how I convinced him to let me be his student. Prof. James is a role model for me. He is a very kind and humble person. I started working with him in his project and I did not know anything about medical image registration. In the first day, he asked me about some mathematical concepts and he gave me the Numerical Recipes in C (The Art of Scientific Computing) book, to read about the minimization or maximization of functions. He was very patient answering and explaining every question on the board. He made sure that I understand every concept in my thesis. This thesis contains a lot of work that requires math, engineering, and medical knowledge. James has been an incredible mentor for me as I developed my mathematical skills. He is always able to give extensive and simple explanations for the hardest concepts. He is a very enthusiastic and energetic person. James has always been an excellent guide for keeping my focus on the application at hand. As I have become more technical in my work, I often find that James's questions are the hardest to answer as he pushes me from thinking about *how* to do something to *why* I'm doing it. His enthusiasm and energy in every meeting was a constant inspiration for me in my career. I really learned from him how to become a real professional scientist, and how to work with scientists from all over the world. I really believe that this experience with James will change my life forever. I also want to thank Sridhar Lakshmanan for his guidance and support. His advices appeared throughout this thesis. I could not have become a successful graduate student without the mentorship of the imaging group team at the radiation oncology department. Even today, much of my understanding of medical image registration comes from conversations I had with Dan Poland and Adam Johansson during my time at the radiation oncology department. They were always patient and enthusiastic with me when I knew so little. The work of Kristy Brock is clear throughout this thesis, and I can happily say that much of my research was spent trying to understand if their ideas could be applied to my work. Finally, I would like to thank my family. My brother Naif has both encouraged me with kind words and inspired me with his own incredible achievements. My lovely sisters and brothers, have inspired me and pushed me to achieve my goal. My mom and dad are everything to me. I'm really trying all my best to make them proud and happy. I love you both.

TABLE OF CONTENTS

LIST OF ABBREVIATIONS

4D CBCT	Four-Dimensional Cone-Beam Computed Tomography
4D CT	Four-Dimensional Computed Tomography
ABC	Active Breathing Control
AP	Anterior-Posterior
CBCT	Cone-Beam Computed Tomography
CCD	Charge-Coupled Device
COM	Centre of Mass
CT	Computed Tomography
CTV	Clinical Target Volume
DTA	Distance to Agreement
EBRT	External Beam Radiotherapy
FEA	Finite Element Analysis
FEM	Finite Element Model
FOV	Field of View
GTV	Gross Tumor Volume
HDPE	High-Density Polyethylene
IGRT	Image-Guided Radiotherapy
IMRT	Intensity Modulated Radiotherapy
LDPE	Low-Density Polyethylene
LR	Left-Right

AP	Anterior-Posterior
SI	Superior-Inferior
MRI	Magnetic Resonance Imaging
ORA	Organ at Risk
PET	Positron Emission Tomography
PTV	Planning Target Volume
QA	Quality Assurance
ROI	Region of Interest
RT	Radiotherapy
MSE	Mean Square Error
CC	Correlation Coefficient
MI	Mutual Information
NMI	Normalized Mutual Information
DVF	Deformation Vector Field

LIST OF FIGURES

LIST OF TABLES

ABSTRACT

Radiation treatment of liver cancer is challenging because the liver and the neighboring organs such as the stomach, small bowel, and esophagus should receive a minimum dose. The localization of the tumor at the treatment session is an important stage to define the dose for the tumor and for the neighboring normal tissue. The localization of liver tumor is very challenging because of the changes to the liver anatomy due to stomach filing, patient positioning, and breathing motion. During breathing, the shape of the liver changes. This change can vary from one person to another and can even vary from day to day for the same person. Image registration can be used to connect treatment images with planning images to define the changes during breathing motion for tumor localization. In this work, thirty patients were studied. First, we created a model for every individual patient by comparing the deformation in the end-exhale position image to that in the inhale position image. Thirty models were created. The displacement field map was calculated for each model, and it was found that the maximum displacement is toward the superior/inferior direction. After that, preprocessing steps for each patient were conducted to create the mean population model. The first step was drawing a manual contour for each end-exhale phase for each patient. Then, one patient was chosen to be the reference patient. After that, the MORFEUS algorithm was performed to align every patient to the reference patient. We did apply linear interpolation to put all patients in the same orientation. We also found the average displacement for the population to create a final global model of the liver. This result will help to improve the treatment of liver cancer.

CHAPTER 1

Introduction and Background

1.1 Treating Liver Cancer

Cancer is one of the main causes of morbidity and mortality around the globe, with approximately 14 million new cases in 2012 [1]. The number of new cases of cancer is expected to increase globally by 70% over the next twenty years. In 2015, cancer was the main cause of death worldwide, with almost 8.8 million deaths [1]. Liver cancer is the second deadliest type of cancer after lung cancer, with more than 788000 deaths [1]. This type of cancer starts in the cells of the liver. The following images show how the liver looks like in 3D viewer [2].

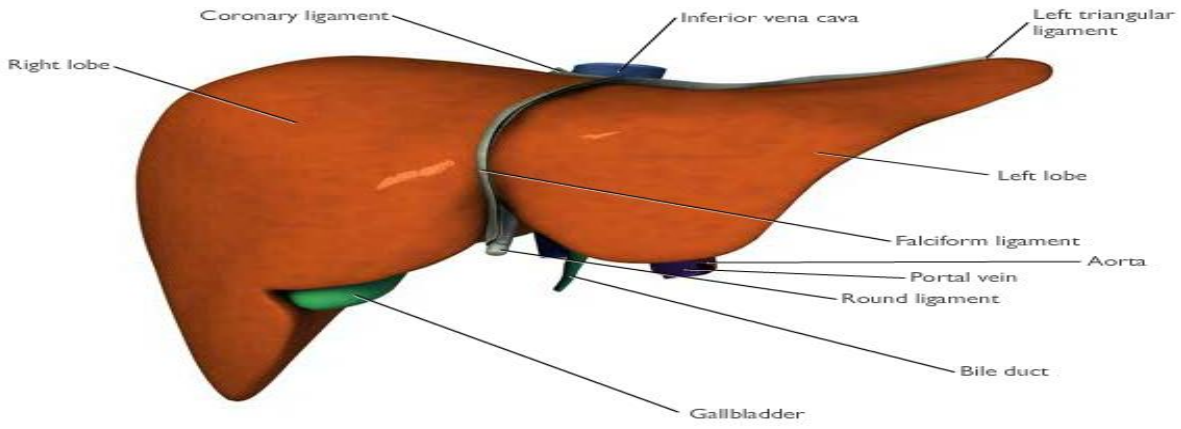

(Figure 1.1.1) Human Liver

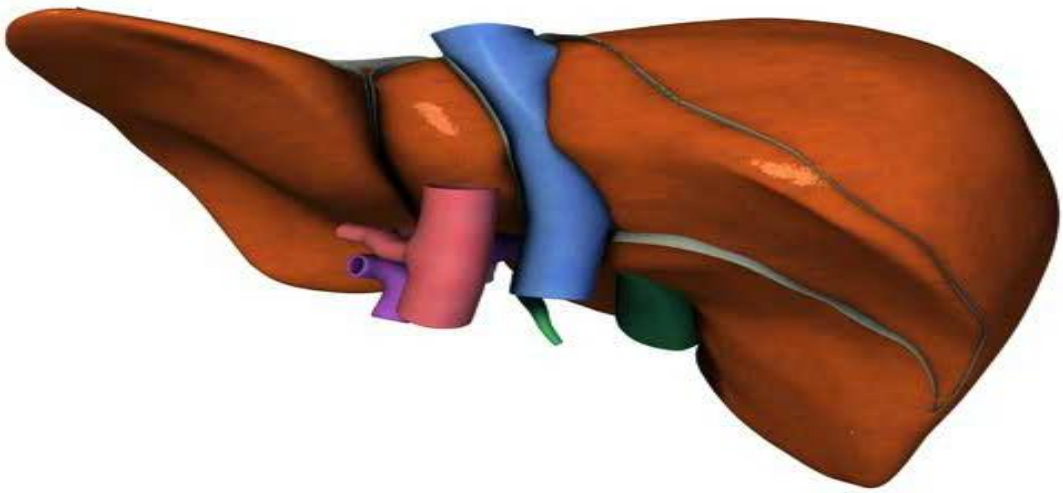

(Figure 1.1.2) Liver (Different View)

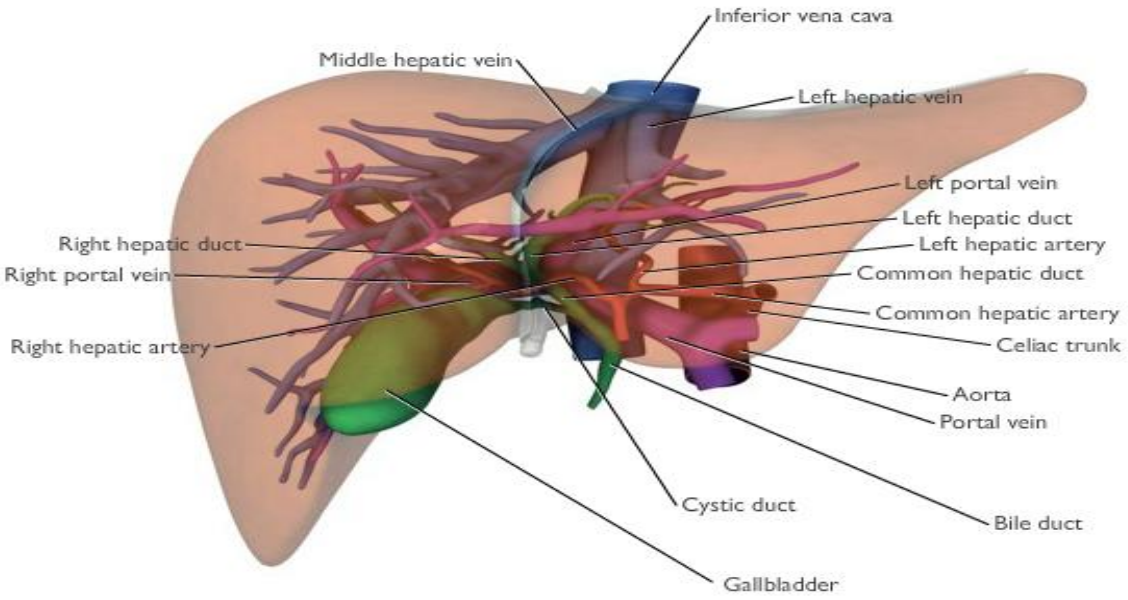

(Figure 1.1.3) Human Liver without the Surface

The following figure shows how the tumor begins inside the liver [3].

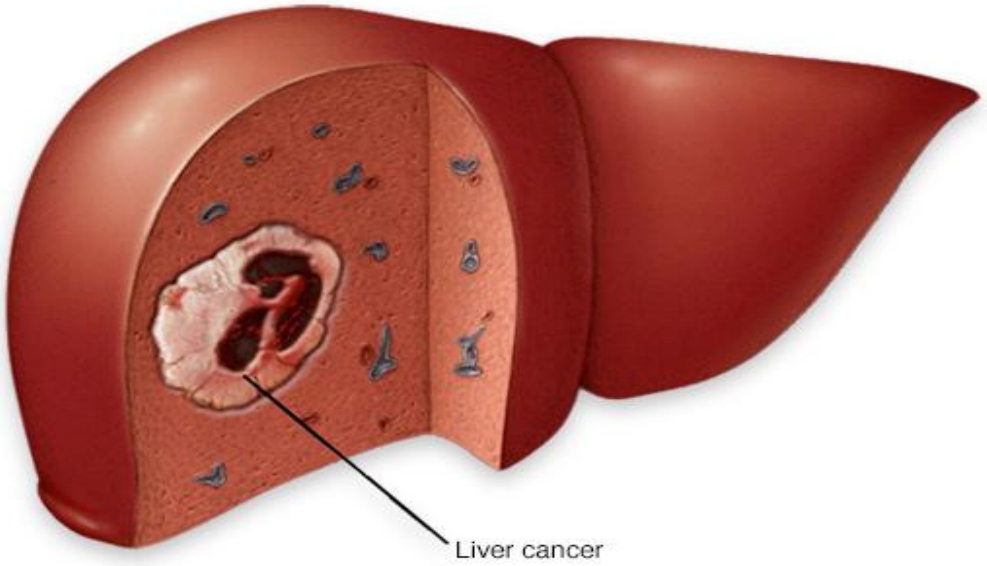

(Figure 1.1.4) Liver Cancer

From the above images, we can conclude that the treatment of liver cancer is very challenging because of the liver's complex network of blood vessels and bile ducts [4].

There are two type of liver cancers. Liver cancers can be both primary and secondary. A liver cancer that starts in the liver is called primary liver cancer [5]. There are many kinds of primary liver cancer, such as hepatocellular cancer, bile duct cancer, angiosarcoma and hemangiosarcoma, and hepatoblastoma [5]. A secondary liver cancer is a cancer that spreads to the liver, but did not start in the liver. Secondary liver cancer comes from the neighbor organs of the liver, such as the pancreas, colon, stomach, breast, or lung. These kinds of tumors are named and treated based on their primary origin [5]. In the USA, secondary liver cancer is more common than primary liver cancer [5]. There are three categories of liver cancer that consider the 5-year survival rate. For localized liver cancer, the 5-year survival rate is almost 31%. For regional stage liver cancer, the

5-year survival rate is about 11%. The 5-year survival rate for distance stage liver cancer is almost 3% [6]. There are three treatment options for liver cancer, namely, surgery, chemotherapy, and radiotherapy. Doctors can combine different options to get better treatment results [7].

1.1.1 Liver Cancer Surgery

Surgery is the essential cure for primary liver cancer [8]. Doctors consider surgery when the cancer is in one area of the liver [8]. Surgery is effective in curing the tumor before it spread to other parts of the body. Many patients are not eligible for surgery because of other diseases and the possible risks and side effects of the surgery. Some people with small liver cancer are eligible for a liver transplant [9]. According to the Organ Procurement and Transplantation Network, almost 1300 liver transplants were done in the United States in 2012 [9].

1.1.2 Chemotherapy for Liver Cancer

Chemotherapy is defined as using anti-cancer drugs to devastate cancer cells [10]. Chemotherapy spreads through the body and attacks any cancerous cells during chromosome duplication or mitosis. The drug can reach directly to the liver by oral means or by injection or can be injected into the bloodstream to circulate around the body [10]. Because the drug circulates around the body, it also attacks also the healthy cells that are dividing quickly, such as the cells in the bone marrow, the lining of the mouth and intestines, and the hair follicles [11]. This can cause some risks and side effects. The common side effects include hair loss, mouth sores, loss of appetite, nausea and vomiting, diarrhea, increased chance of infections, easy bruising or bleeding, and fatigue [11]. Some doctors use chemotherapy in conjunction with embolization, which means blocking one of the liver's arterial blood supplies to starve the tumor, but this will also destroy some healthy tissue [12].

1.1.3 Radiation Therapy for Liver Cancer

The X-ray, an electromagnetic wave of high energy radiation, was discovered by German physicist Wilhelm Roentgen [13]. The use of X-rays in diagnosis and treatment of diseases makes them very important for the medical field. X-rays can penetrate through many objects, which helps in forming images. This is the main concept of X-ray imaging of the body. Scientists later found that X-rays can kill cancer cells and shrink tumors because of the high-energy emission. Radiation therapy uses X-rays, gamma rays, and other sources of energy radiation to kill cancerous cells [13]. Radiation destroys cells by damaging their DNA [13]. The cells can be destroyed straightaway, or some certain parts of cells, such as their DNA, can be killed, thereby making the cell no longer able to divide [13].

In radiotherapy treatment, complicated equipment produces a high-energy beam, such as X-rays, gamma rays, and others. Patients lie down on the bed under the machine, and the beams are focused on the cancer target [13]. Before starting the treatment, a radiation oncologist establishes a treatment plan for every patient. This process is called treatment planning, which starts with simulation [14]. During this planning, precise imaging scans display the exact location of the tumor and the organ edges to differentiate between the healthy and unhealthy tissue. There are many scans involved in this process, such as computed tomography (CT), magnetic resonance imaging (MRI), position emission tomography (PET), and ultrasound scans [14]. The following image shows a CT scan machine [15].

(Figure 1.1.3.1) Computed Tomography Scanner.

CT scans are often used in treatment planning for radiation therapy. During CT scanning, pictures of the inside of the body are created by a computer linked to an X-ray machine [14].

During simulation and daily sessions, it is important to keep the patient in the same position and to use body molds and masks [16]. After simulation, the doctor decides what the treatment target is, how much the dose is for the tumor and for the normal area, and what the best angle is at which to deliver this dose [14].

There are three main kinds of radiation therapy. The first one is external beam radiation therapy. In this type, the radiation dose is delivered from a machine outside the body with a specific distance and taking all the information from the treatment planning and making sure the dose is focused on the target. There are many systems that generate different kinds of radiation for external beam therapy, such as orthovoltage x-ray machines, Cobalt-60 machines, and linear accelerators [13].

Linear accelerator treatment is referred to as external beam radiotherapy (EBRT) because the radiation source is outside the patient's body. In radiotherapy treatment, radiation kills both cancerous cells and normal cells. This has imposed a great challenge in using EBRT to treat liver cancers, because normal liver tissue has a low tolerance to ionizing radiation. It has been shown that a dose of 120 Gy is required to kill a primary liver tumor, while the surrounding normal hepatic tissue can tolerate only 30 to 35 Gy. Doses beyond this limit might cause radiation-induced liver disease (RILD), which includes venal occlusion in the liver and hepatocyte atrophy [24]. Accurate and precise targeting is therefore required to deliver a high dose to the tumor while sparing the surrounding healthy tissues as much as possible. The second kind of radiation therapy is internal radiation therapy, which is called brachytherapy. In this type, a radiation source is placed inside the body and sometimes inside the tumor tissue [14]. This type is effective in treating some types of cancers, such as cervix, uterus, vagina, rectum, eye, and certain head and neck cancers [13]. The third type of radiation therapy is proton therapy. In this type, the radiation waves do not go through the body and are just focused on the tumor and stopped there [17]. Currently, proton therapy is used to treat prostate cancer, lung cancer, head and neck cancers, liver cancer, bile duct cancer, and pediatric tumors [17].

There are three goals of radiotherapy treatment. Radiotherapy goals are curative, adjuvant, and palliative treatments, depending on the treatment intent. The target of curative radiotherapy is to eliminate the tumor with a high dose, which requires high-precision localization [13]. Adjuvant radiotherapy supports surgery with a low dose. The aim of palliative radiotherapy is to mitigate cancer symptoms and slow down its growth. Doctors decide the dose level of palliative radiotherapy according to the disease conditions and what treatment is required [18].

1.1.4 Tumor Ablation for Liver Cancer

Ablation is treatment that destroys liver tumors without removing them [19]. Doctors use this method when there is a small tumor and when the patient is in bad health and sometimes for a patient who is waiting for a liver transplant [19]. This method is very effective for tumors no larger than 3 cm. Doctors can combine this method with embolization for larger tumors (3 to 5 cm across) [19].

1.1.5 Embolization Therapy for Liver Cancer

In this method, doctors try to reduce the blood flow to cancer cells in the liver by injecting some materials. This way of treatment will not harm the health of the cells of the liver because these cells will get their blood supply from the portal vein [20]. Embolization is good for patients with liver cancer larger than 5 cm across, and it can be used with ablation [20].

1.1.6 Targeted Therapy for Liver Cancer

After the discoveries of the changes in the cells that cause cancer, researchers have been able to develop new drugs that target just the changes in these cells [21]. This method is a very active treatment option because of its fewer side effects compared to chemotherapy. Doctors are looking to this method as a promising and effective way to treat liver cancer.

1.2 Treatment Planning of Radiotherapy

1.2.1 Treatment Planning Simulation

Before starting the radiotherapy treatment, patient goes through a treatment planning process called radiation simulation [22, 23, 24]. Treatment planning usually involves positioning the body, making marks on the skin and taking imaging scans. An image of a patients' internal anatomy is acquired by using different kinds of medical imaging modalities such as fluoroscopy, computed

tomography (CT), magnetic resonance imaging (MRI), and positron emission tomography (PET) [25]. CT simulation contains a CT scan of the area of the body to be treated with radiation. The CT images acquired during the scan will be reconstructed and used to evaluate and design the most precise treatment planning. The simulation part of the radiotherapy treatment confirms that treatments will destroy the target, while missing surrounding critical structures [26]. Nowadays, MRI became more popular in radiotherapy treatment planning and is used to provide better soft tissue contrasts to enable a clearer visualization of the tumor. Since geometrical distortions can occur in MR images, they are always correlated to the CT images through the process of image registration [25]. Simulation can be classified to 2D, 3D (CT, MRI), or 4D (respiration correlated CT or 4D CT), depending on treatment intent and the size, shape, and the location of the tumor [27].

1.2.2 Images Delineation on Treatment Planning

The organ at risk (OAR) is the nearby healthy structures that are sensitive to radiation. There are two kinds of the physiological functions of a structure in the body, serial and parallel. The serial function such as neural signal conduction, are permanently deteriorated if the corresponding anatomy, such as the spinal cord, is damaged [25]. For this function, when planning the treatment, the dose should be minimized to the OAR structure. For parallel functions, these functions can be restored when they partially destroyed. For example, the liver can work perfectly when part of it is removed. For parallel structures, the dose of the healthy tissue is minimized as possible.

After getting the simulation images, the radiation oncologist evaluates them and contours a gross tumor volume (GTV), which is the visible tumor mass on the images, and a clinical target volume (CTV), which adds a margin around the GTV to include the filtration of cancerous cells into the surrounding tissues that is not visible on images [25]. Then a radiation therapist creates a planning

target volume (PTV), which further expands the CTV to account for possible geometric localization errors and changes in tumor position and OAR position [28] (See Figure 1.2.2.1).

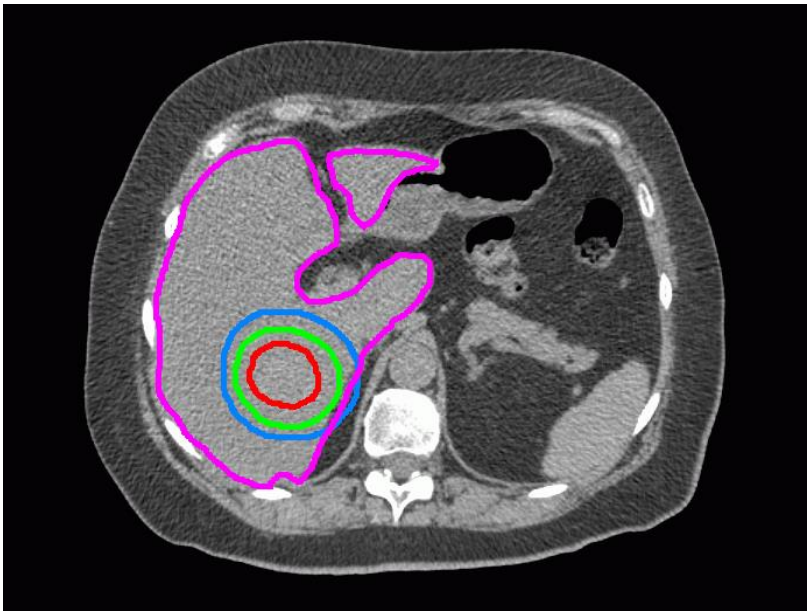

(Figure 1.2.2.1) CT Image of a Liver Cancer Patient with Target Volumes (GTV(red), CTV(green), PTV(blue), Contour of the liver (pink))

PTV is the region that cover the geometric treatment uncertainties including respiration-induced tumor movements and patient positioning errors.

1.2.3 Prescription and Calculation of the Dose

Region of interest is the target of the radiation dose and is prescribed to it. 95% of the PTV is covered with at least 95% of the dose and the OAR must receive a dose below their tolerance [28]. The following figure shows how the conformal radiation therapy, particularly intensity modulated radiation therapy (IMRT), uses to optimize beam arrangement and the delivery of radiation [29].

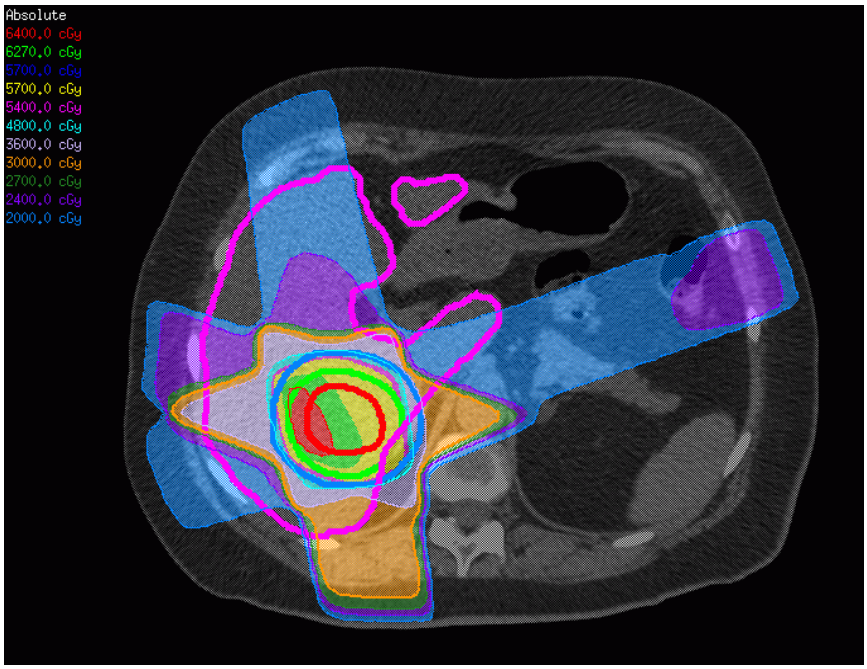

(Figure 1.2.2.2) Simulated Beam Arrangement with Dose Distribution of a Conformal RT Plan on the CT Image for Liver Cancer Patient

PTV receives the high dose and the dose is minimized as possible for healthy tissue in the liver.

1.3 Patient Anatomy Displacement in RT

The treatment plans in radiation therapy usually stay the same throughout the period of treatment. We know that the treatment planning takes several sessions called fractions. It is an important to ensure that the target tissue and OARs are at the same spot in each fraction of the treatment planning. Unluckily, the position and geometry of both the tumor and the OARs would unavoidably change between the time of planning and the time of delivering the treatment, between fractions (i.e. inter-fractional displacement), and during a fraction (i.e. intra fractional displacement) [25]. These changes can affect the ultimate goal of the treatment, which is the 95% of the dose to the PTV. The errors of not targeting the PTV and deliver more dose outside this area can push the OAR and the healthy tissue inside the high dose region [30]. Therefore, considerable

efforts have been dedicated to developing accurate tumor targeting techniques to accommodate for inter-fractional and intra-fractional displacements [31, 32].

1.3.1 Inter-Fractional Variation

Inter-fractional variations in patient anatomy and tumor position can be defined as the patient setup and image guidance techniques [25]. Creating a common coordinate system for treatment planning and delivery is very helpful in getting patient setup. The coordinate system is defined by the radiation isocenter, which is the converging point of radiation beams delivered from different directions. The isocenter is identified by three intersecting orthogonal laser beams in the treatment room, and is replicated by another set of three orthogonal lasers in the simulation room [25]. Using some kind of marks in the body such as symbols drawn with ink and using laser beams helps a lot in keeping patient positioning at each session of treatment. Immobilization devices are often used to facilitate the reproduction of patient position from the time of planning to the last treatment fraction [33].

In image-guided radiotherapy (IGRT), the patient is imaged with a 3D cone-beam CT (CBCT) installed in the treatment room immediately before each fraction. Surrogates are utilized in CBCT images to represent the tumor position because the tumor does not show on CBCT due to contrast limitation. There are many examples of the common used surrogates contain natural anatomical landmarks such as bony structures and vascular bifurcations, or artificially implanted fiducial markers such as gold seeds for prostate cancers [34]. With the improvements of the image technologies which result in an improvement on soft tissue contrasts, we could visualize organs such as the liver on CBCT images. We can identify the position of the tumor using image registration. When using rigid registration for tumor localization, they assume that the movements of the tumor is the same as the surrogates and this is not always true [34]. Another option is the

deformable image registration, which can be used to align CBCT images with the planning image. More explanations about deformable image registration will be discussed later.

During treatment session, tumors and normal tissues may respond to radiation and then shrink or expand, which also participate to inter-fractional variations [34].

1.3.2 Intra-fractional Variations

Motions due to physiological processes, such as breathing, is the cause of intra-fractional organ displacements. During breathing, liver can be deformed by a few centimeters, which leads to errors during the delivery of radiations. Target organ and tumor movements due to breathing can be addressed by PTV margin expansion, image guidance, gated beam delivery technique, and breathing motion control [34]. The PTV area guarantees that the volume of the tumor is covered by the high dose level. To study any tumor displacements by image guidance, this requires imaging the patient with 4D CBCT at each fraction [34]. The 4D CBCT images can be correlated with different phases of the breathing cycle. The image corresponding to inhale can be mapped with the image corresponding to exhale via deformable image registration, enabling characterization of a patient's breathing motion at the time of treatment [34].

1.4 Medical image registration

In this section, medical image registration is discussed. It is known that the goal of image registration is to align the corresponding features in some images with respect to a reference image [43]. There are many applications of medical image registration such as tumor localization, image guided, surgery, and many more. There are different methods to perform image registration. These methods can be classified depending on the number of criteria as illustrated in the following figure [43].

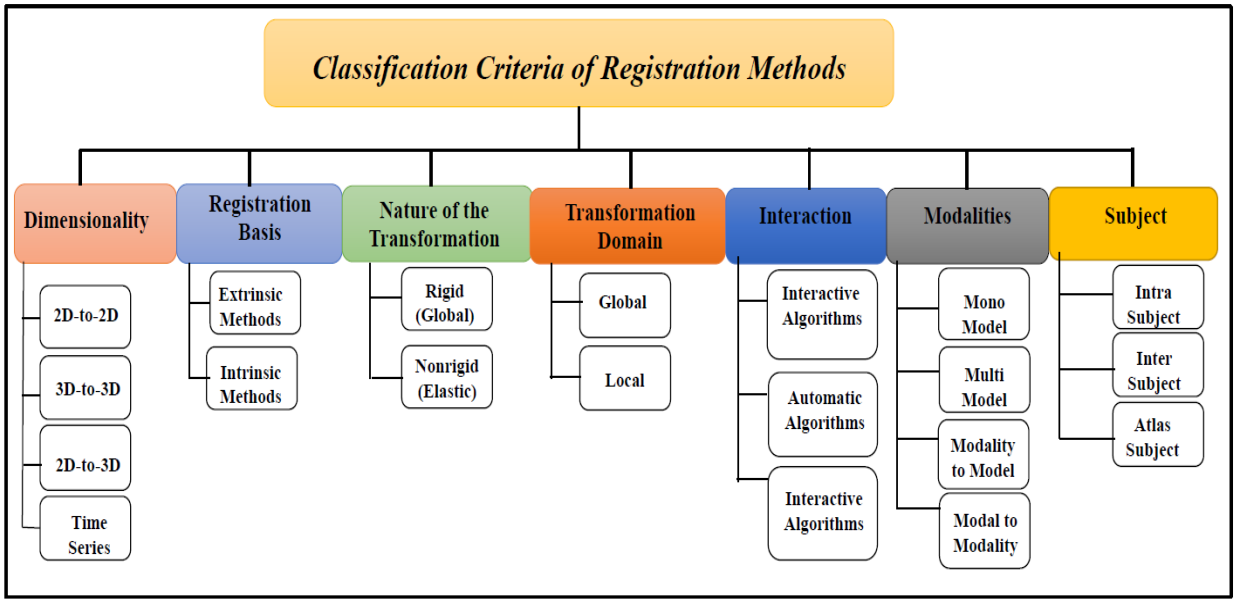

(Figure 1.4.1) The classification criteria of the registration methods

1.4.1 Dimensionality

This standard is classified into spatial and time-series dimensions. In spatial dimensions, image dimensionality refers to the number of geometrical dimensions of the image space. In this criterion, the registration might be done based on a group of corresponding point pairs or a set of corresponding surface pairs [43].

1.4.2 Registration basis

The registration under this criterion are categorized based on the nature of the registration basis into extrinsic and intrinsic methods. In extrinsic registration methods, some visible artificial objects are attached to the patient and should be detectable in all the acquired modalities. In intrinsic registration methods, some information from patient are provided such as apparent prominent landmarks, binary divided structures or voxel image intensities [44].

1.4.3 Nature of the transformation

This standard is categorized to two methods: rigid (global) and non-rigid (elastic/local) transformations [43]. In the rigid transformation methods, the entire 2D or 3D images are

transformed, translating, rotating, scaling and/or sharing every depicted object in the same way that in turn preserves distances, lines and angles [45,46]. The application of non-rigid registration is ranging from modeling tissue deformations anatomical structures' variability. The complexity of non-rigid registration and the need of the smoothness and the high degree of freedom in the deformation process make it an open research area [43].

1.4.4 Transformation domain

The coordinate transformation of the images can be classified to global or local. In the global case, the transformation is accomplished by mapping the valid parameters for the entire image. In the local method, part of the image is transformed considering that the local mapping function parameters are valid for this part [47].

1.4.5 Interaction

The interaction between user and image registration process in image registration is classified to three level of interactions. In interactive algorithms, the user uses a software to perform the registration by inserting every parameter. In automatic algorithms, no interactive is required and all the work is done automatically [43]. I semi-automatic algorithms, the user applies the algorithm initializations desired through segmenting the data or steering the algorithm to the solution [47].

1.4.6 Modalities

In this method, there are four methods of registrations based on the kind of modalities. Mono-modal means performing the registration of the same medical modality. In multi-modal methods, different modalities are used. In modality to model and model to modality registration tasks, only one image is included while a model is the other registration input.

1.4.7 Subject

This represents the patient whose images are to be registered. For intra subject, the registration is accomplished for images from the same subject. For inter subject registration methods, different patient images are involved in the registration. For atlas based registration methods, a single patient image with another image constructed through a database of image information acquired via many subjects imaging [43].

1.5 Quantification of liver motion: deformable image registration

Images registration is very useful in radiation therapy to measure the quantity of liver motion and to transfer the planning situation into the treatment scenario [48]. In general, image registration is an optimization process for determining a spatial transformation relating the position in one image (reference or fixed image) to the corresponding position in one or more other images (target or moving image) [48]. The following image shows the image registration workflow [48].

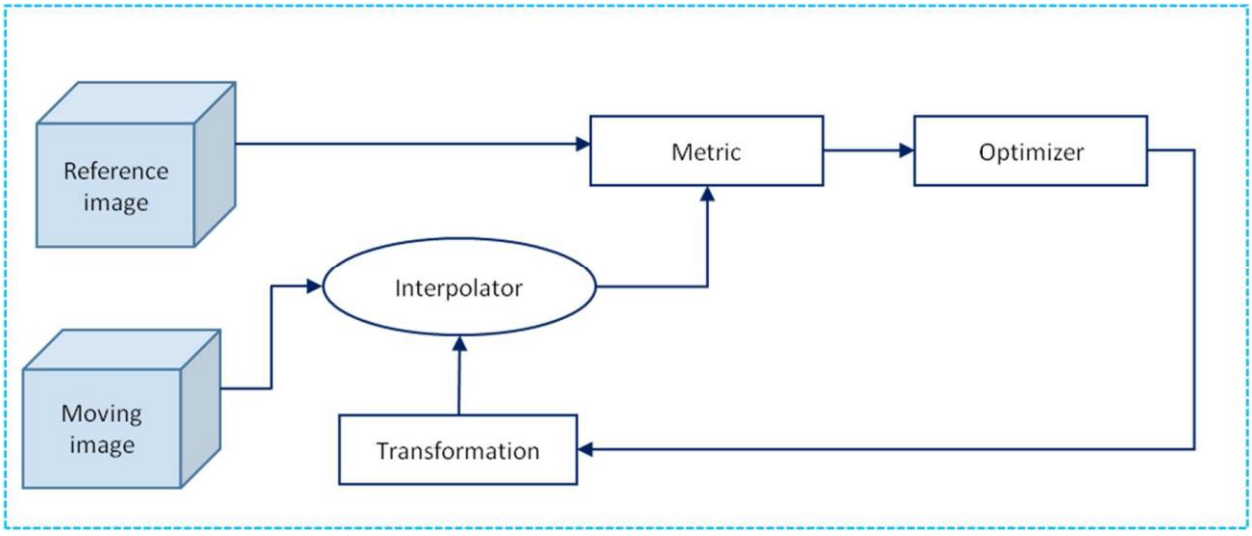

(Figure 1.5.1) Image registration workflow

From the image registration workflow figure, the interpolator transforms the coordinates of the floating image into the physical space of the coordinates of the reference image [48]. The metric

determines the similarity metric between the two images considering the modalities of the registration. The similarity metrics for mono-modal images are the mean square error (MSE) and the correlation coefficient (CC) [48]. Moreover, the similarity metrics for multi-modal images are mutual information (MI) and normalized mutual information (NMI) [48]. In this project, we used the mono and multi modalities similarity metrics. The optimizer calculates the optimal parameters of the transformation in order to maximize/minimize the similarity/difference between the reference and the floating image. The transformation as we discuss it above can be divided in global, applied on the entire image, or local, applied to subsections of the images. The transformations can be subdivided in rigid, affine and deformable [48]. The following figure shows the type of transformation [48].

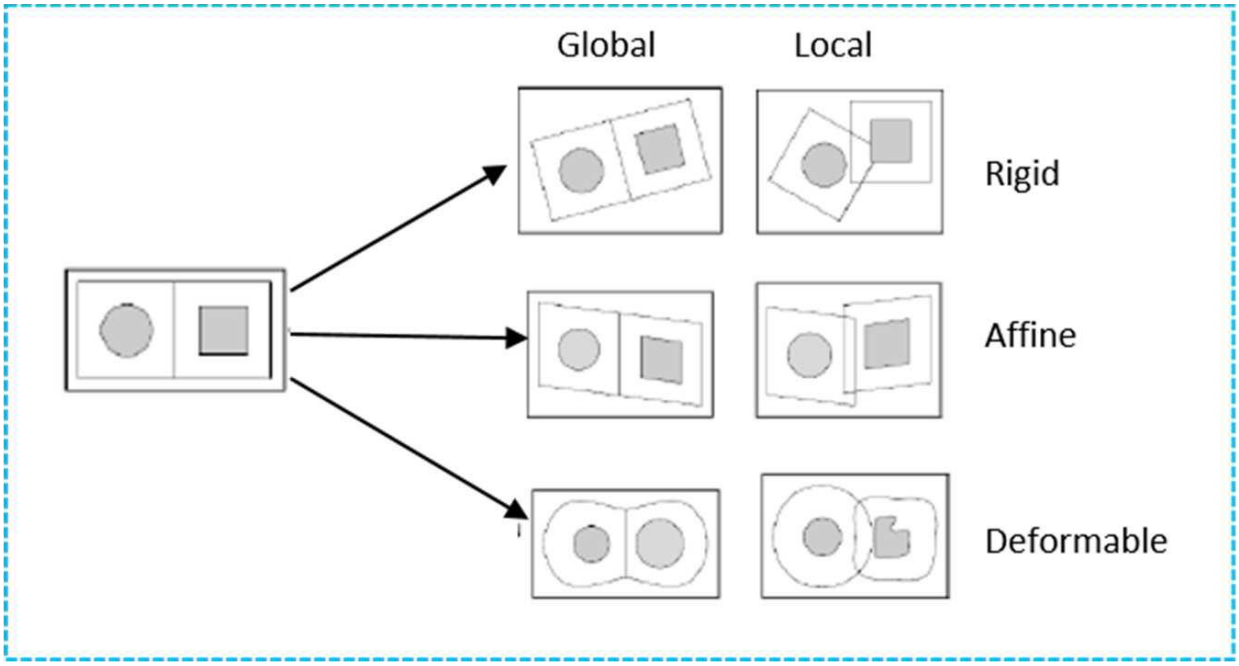

(Figure 1.5.2) Type of transformation

Deformable image registration (DIR) is used to take into account deformation due to the non-rigid nature of the patient body. The output of DIR is described by a deformation model, known as deformation vector field (DVF), which refers the displacement between each voxel in the reference image and each corresponding voxel in the target image [48]. There are many ways to calculate

DVF such as: thin plate splines, radial basis functions (RBF), Demons (based on the intensity conservation between reference and moving image) and free-form deformation (FFD) based on B splines [48]. We used in this project the B-Splines based deformable registration and demons. The B-Splines based deformable registration applies a B-spline grid onto the voxel grid of the image [48]. This algorithm gets interpolated DVFs as result of the interpolation of the B-spline grid on the voxel-grid [49]. Figure 1 shows the B-Spline DIR [49].

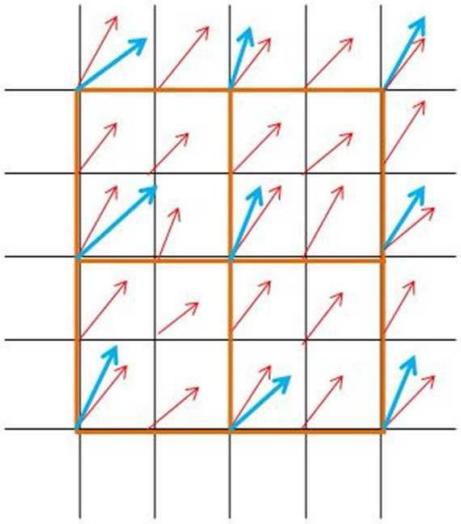

(Figure 1.5.3) B-Spline DIR: B-spline grid (in orange) applied on the voxel grid (in black) with its vectors (in red) and the resulting interpolated vector field (in light blue).

To get the DVF, the following equation is applied [49]:

$$v(x,y,z) = \sum_{i=1}^{4}\sum_{j=1}^{4}\sum_{k=1}^{4} P(i,j,k)B_i(x)B_j(y)B_k(z) \qquad (1)$$

Where:

$B_i(x)B_j(y)B_k(z)$: basis pre-calculated of the B-spline

$P(i,j,k)$: B-splines coefficients to be optimized.

CHAPTER 2

Modeling Inhale to Exhale for Individual Patients

2.1 Introduction

Computed tomography (CT) and cone-beam CT (CBCT) scans are the clinical standards these days for treatment planning and position verification [35]. However, abdominal lesions are hard to view on these images because of the inadequate soft-tissue contrast from (CB)CT. In addition, breathing movement in the upper part of the abdomen makes it hard to get accurate images and to deliver doses. Thus, all treatments of a cancer tumor in this area, such as in the liver, need a large safety margin and set-up fiducial markers. These days, MRI has become more popular for treatment planning and image guidance because of the superior soft-tissue contrast that MRI provides [35]. An integrated MRI scanner with a linear accelerator (MR-linac) will help in the future to view abdominal lesions on the treatment machine. This could potentially lead to more accurate dose delivery facilitating margin reduction or dose escalation [35]. Thus, new MRI-based strategies for radiotherapy of moving targets are required [35]. There are many ways to measure breathing motion in radiotherapy. Gating and tracking are considered accurate methods but require real-time tumor localization and linac response [36,37]. Motion-encompassing techniques such as

the internal-target-volume method (ITV) or strategies based on irradiation of the time-weighted mean position of the tumor only affect the treatment preparation phase and are therefore relativelyeasy to use clinically [38]. Non-rigid image registration is used also to align to the images and consider the orientation and the breathing motion. We address the problem as modeling of the inhale to exhale of the individual patient. To tackle this problem, a non-rigid registration algorithm is needed to deal with the breathing motion and the orientation of the images. The fast-free form deformation for non-rigid registration algorithm was used to produce this model. This algorithm was established by Daniel Rueckert [39] and re-factored by Marc Modat et al [40]. In this algorithm, cubic B-Spline is used to deform a source image to optimize an objective function based on the Normalized Mutual Information and a penalty term [40]. The penalty term can be either the bending energy or the squared Jacobian determinant log [40]. This method has the desirable feature of guaranteeing a C^2 continuous deformation.

2.2 Method

Using MRI images acquired from thirty patients, an individual model for each patient was created. Each patient was provided with the breathing cycle from start-inhale position to end-exhale position. For this study, the start-inhale position image was chosen to be the reference phase and the end-exhale phase to be the floating image. This is the largest displacement for each patient, which is of interest of this study. The steps in performing the registration using this algorithm are shown below. In the following section, the method of modeling the inhale to exhale for an individual patient is presented. The data that were used for this work are from thirty patients; a summary table is created at the end to show all the results.

2.3 Discussion

2.3.1 Modeling the start phase of inhale to the end phase of exhale for Patient 1

Every patient has twenty-one images for the breathing cycle, starting from inhale to exhale. Upon choosing the start phase of inhale and the end phase of exhale, registration was performed. To apply the previous algorithm, a reference image and a floating image were assigned. The reference image is the start phase of inhalation and is shown below.

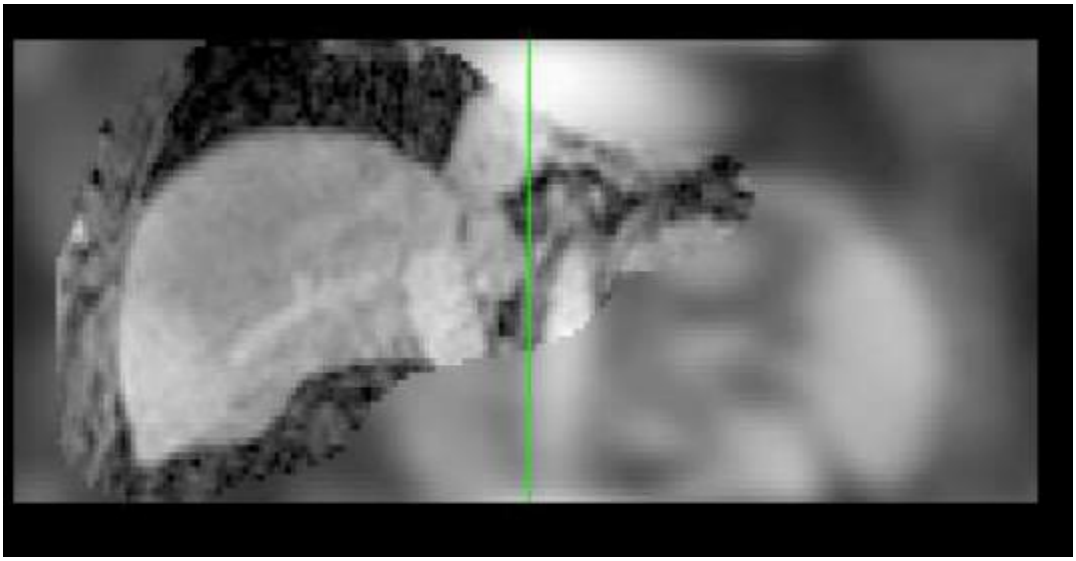

(Figure 2.3.1.1) Inhale Phase of Patient 1

Part of the image in Figure 2.3.1.1 is blurred to be able to get an accurate view of the liver. The deformed image is the end phase of exhalation and the image is shown below.

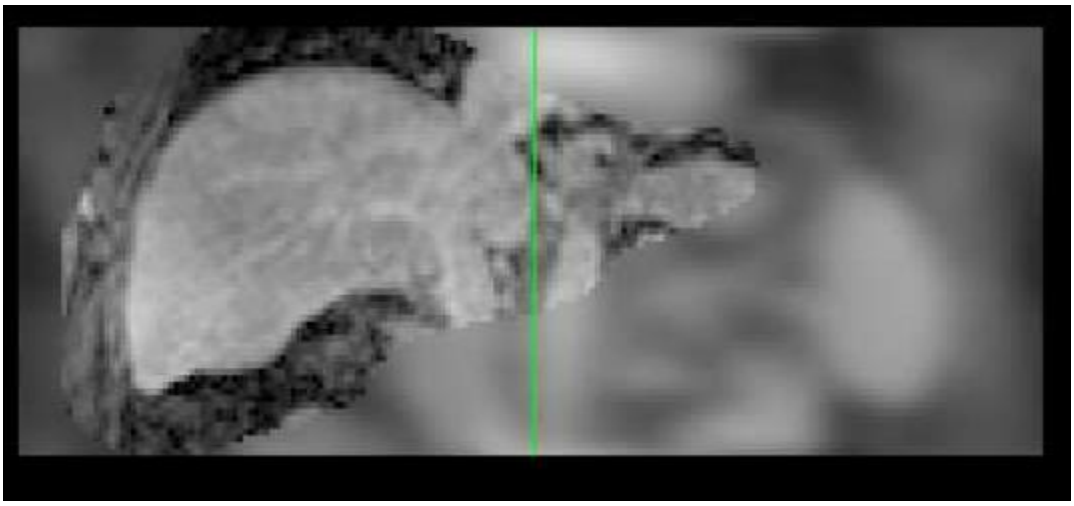

(Figure 2.3.1.2) Exhale Phase of Patient 1

To determine how much displacement occurs to the liver during breathing through the inferior and superior, right and left, and anterior and posterior, the fast free-form deformation algorithm for non-rigid registration is performed. The output of this algorithm is the control point grids and the resampling image. The control point grids are the number of corresponding control points. The control point grids are then converted to deformation fields with the availability of the reference image to get the deformation field. After that, the transformation function is determined to get the correspondence between the remaining points in the images. The last step is calculating the displacement field by transferring the deformation field to the new displacement field. The displacement field map shows how much displacement there is through the x, y, and z axes in millimeters.

The following image is the resulting volume of the displacement map after using MATLAB to upload this map as an array volume to represent its coordinate system.

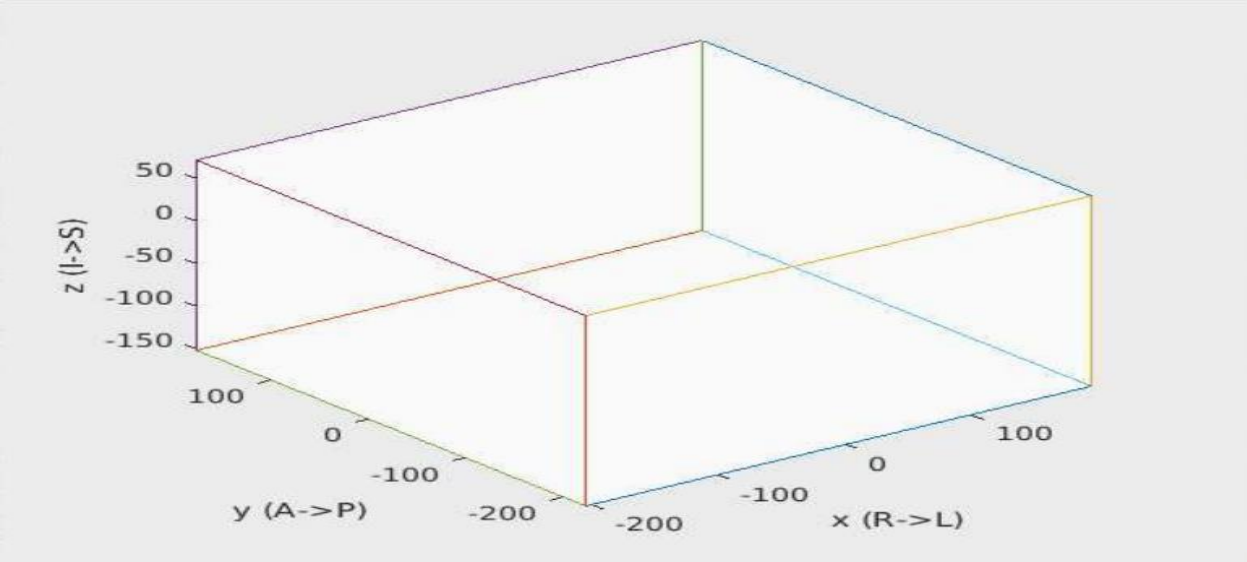

(Figure 2.3.1.3) Volume of the Displacement Map of Patient 1

Figure 2.3.1.3 shows also the coordinate system of the displacement map. Z-axis is superior (+) and inferior (-). X-axis is left (+) and right (-). Y-axis is posterior (+) and anterior (-).

The histogram of this map is below.

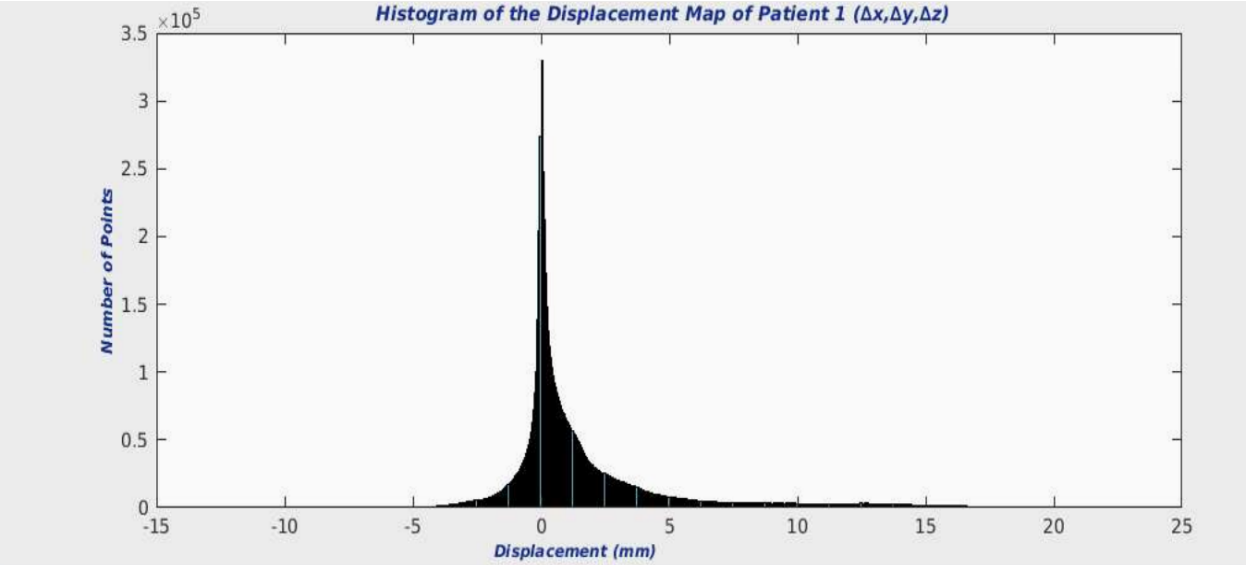

(Figure 2.3.1.4) Patient 1 Displacement Map Histogram

The displacement is between approximately -5 mm and 15 mm. The maximum displacement happens between approximately -5 mm and 5 mm. The following steps are the process of analysis of each axis of the displacement map. From the above histogram, almost 80% of the displacement occurs toward the left direction.

For analysis purposes, the displacement map was separated into individual axes. The following image shows the Δx displacement map.

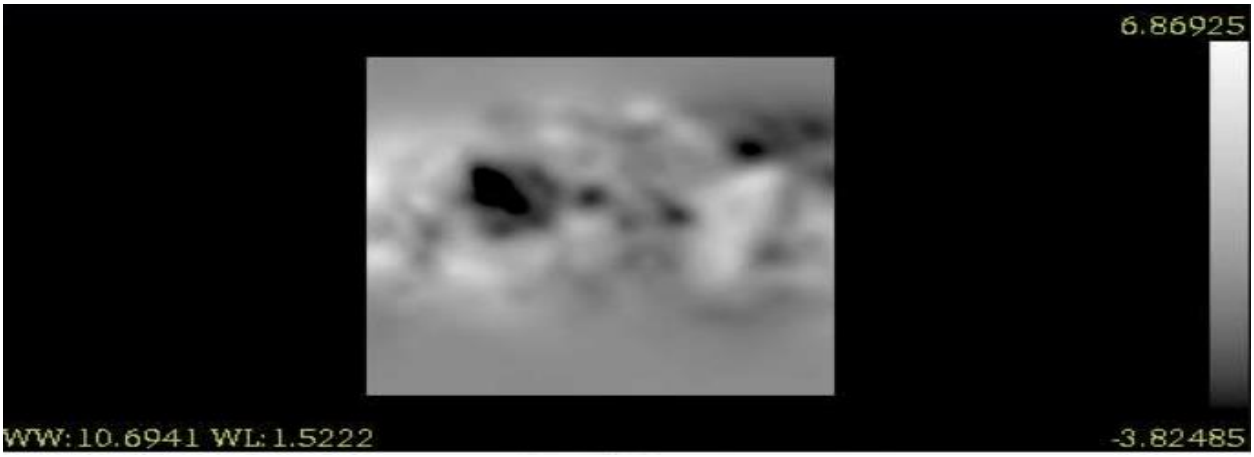

(Figure 2.3.1.5) Patient 1 Δx Displacement Map

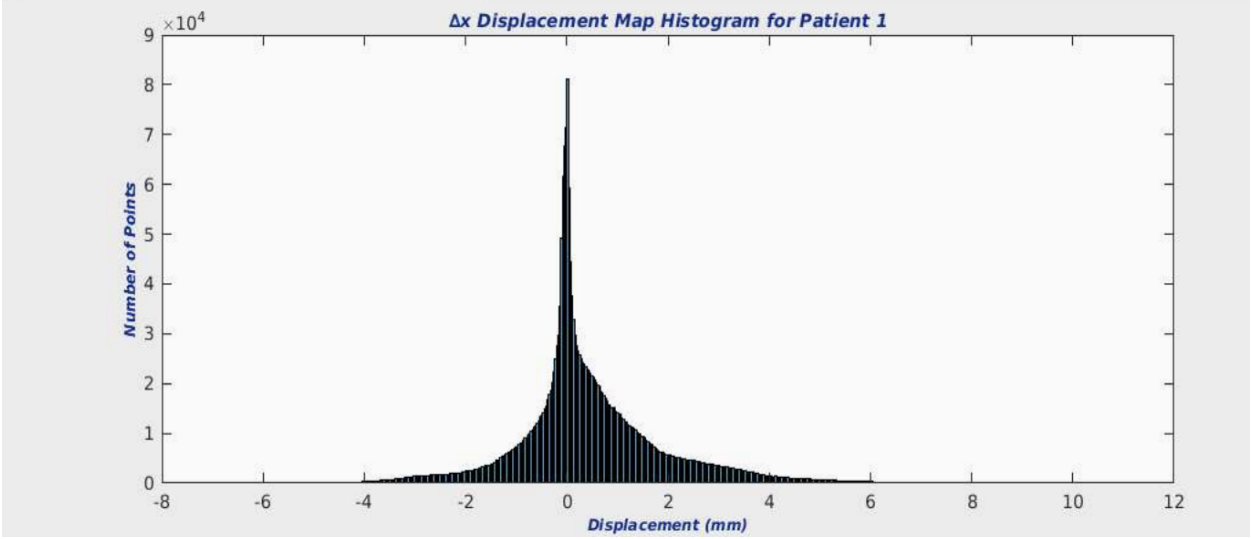

(Figure 2.3.1.6) Patient 1 Δx Displacement Map Histogram

From the Δx displacement histogram, the highest displacement is in middle area of the histogram. From the graph, there is more displacement toward the left direction compared to the right direction.

The following figure shows the Δx Displacement Mean through the x spacing of the entire image of the Δx displacement field.

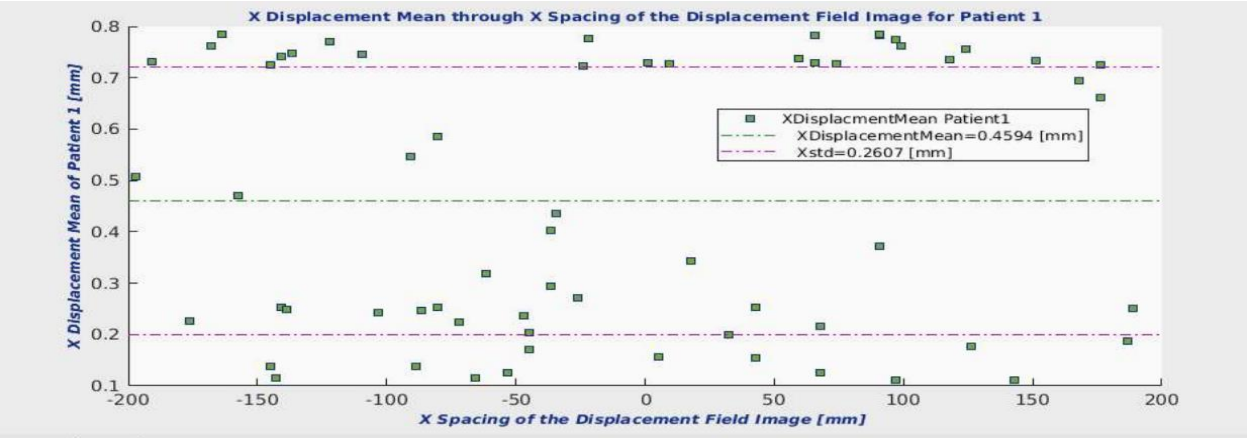

(Figure 2.3.1.7) Δx Displacement Mean and x Spacing of the Displacement Field Image

The Δx displacement mean is shown to be 0.4594 mm and the standard deviation is 0.2607 mm. This shows that the displacement toward the right/left direction is not that high and the displacement toward the left is higher than to the right direction.

For Δy displacement, the following image shows a screenshot of this displacement map.

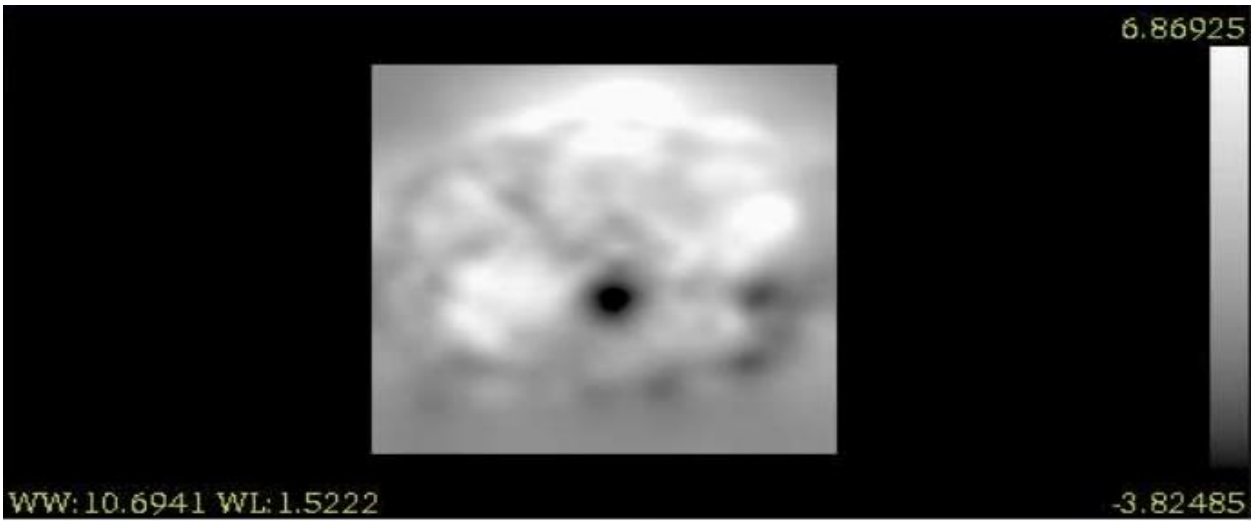

(Figure 2.3.1.8) Patient 1 Δy Displacement Map

The following histogram represents all the data inside the Δy displacement.

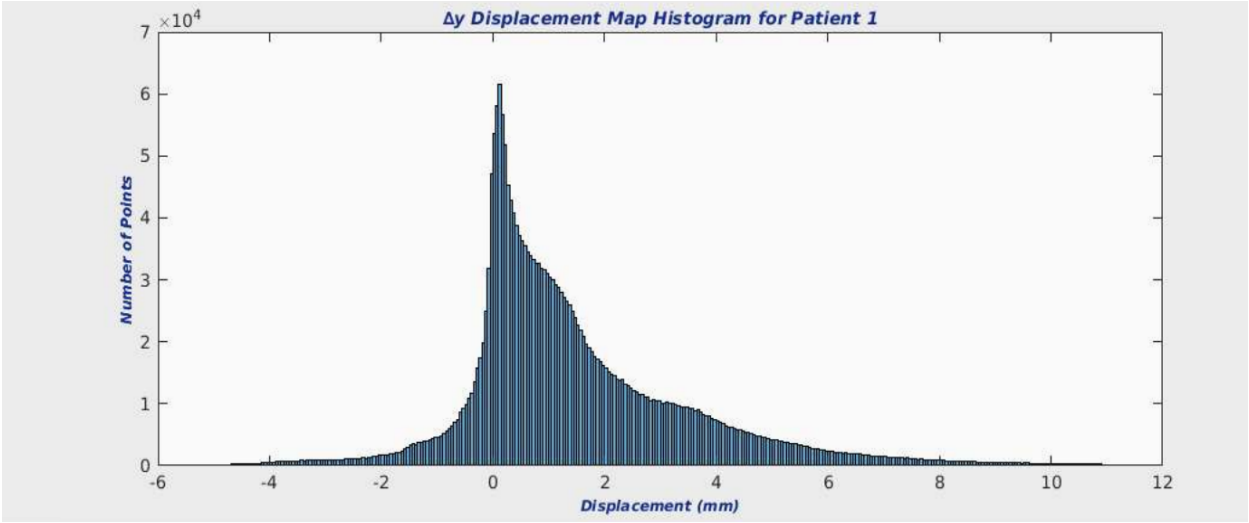

(Figure 2.3.1.9) Patient 1 Δy Displacement Map Histogram

From the Δy displacement histogram figure, most of the displacement is approximately between 0 mm and 8 mm. This means that more displacement occurs toward the posterior direction. The number of points or the frequency gives information about how much displacement occurs through this axis compared to the other axes.

The following map shows the mean of the Δy displacement in the posterior/anterior direction. The Δy displacement mean equals 1.482 mm and the standard deviation is 0.6969 mm, which is higher than the Δx displacement.

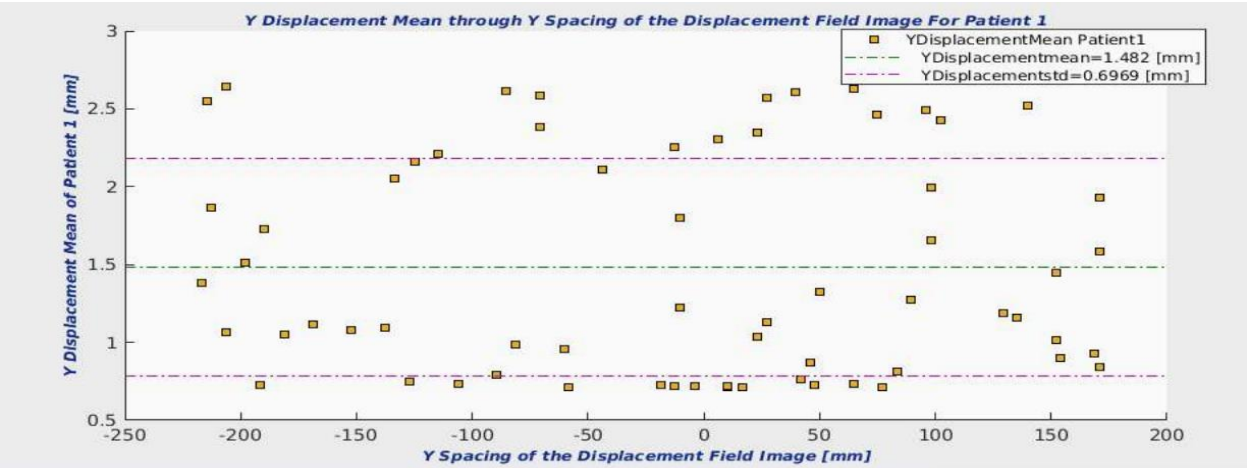

(Figure 2.3.1.10) Δy Displacement Mean and y Spacing of the Displacement Field Image

In Figure 2.3.1.10, the Δy displacement mean equals 1.482 mm and the standard deviation is 0.6969 mm, which is higher than the Δx displacement.

The last part of the displacement map is the Δ*z* displacement map (Figure 3.3.1.11).

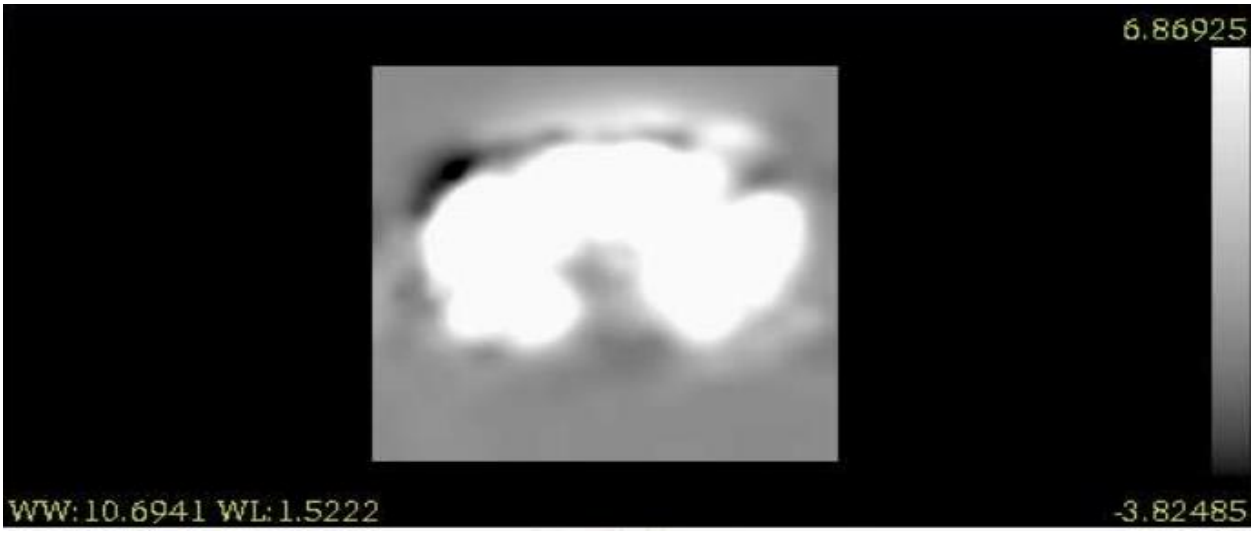

(Figure 2.3.1.11) Patient 1 Δz Displacement Map

To represent and analyze the Δz displacement map, the histogram of this image was calculated (Figure 2.3.1.12).

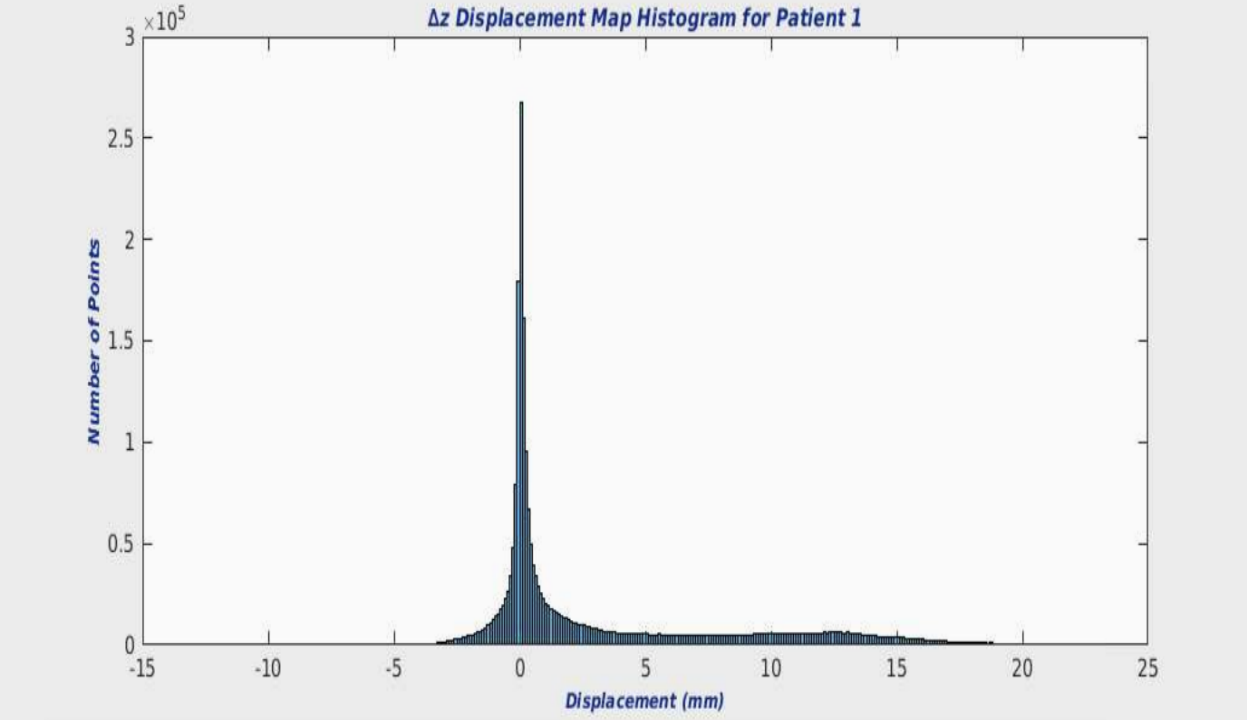

(Figure 2.3.1.12) Patient 1 Δz Displacement Map Histogram

In Figure. 2.3.1.12, most of the displacement occurs in the superior direction. The number of points in the y axis, which is called the frequency, is very high compared to the Δx and Δy displacements.

The following figure shows the mean of Δz displacement in the y axis and the SI coordinate in the x axis.

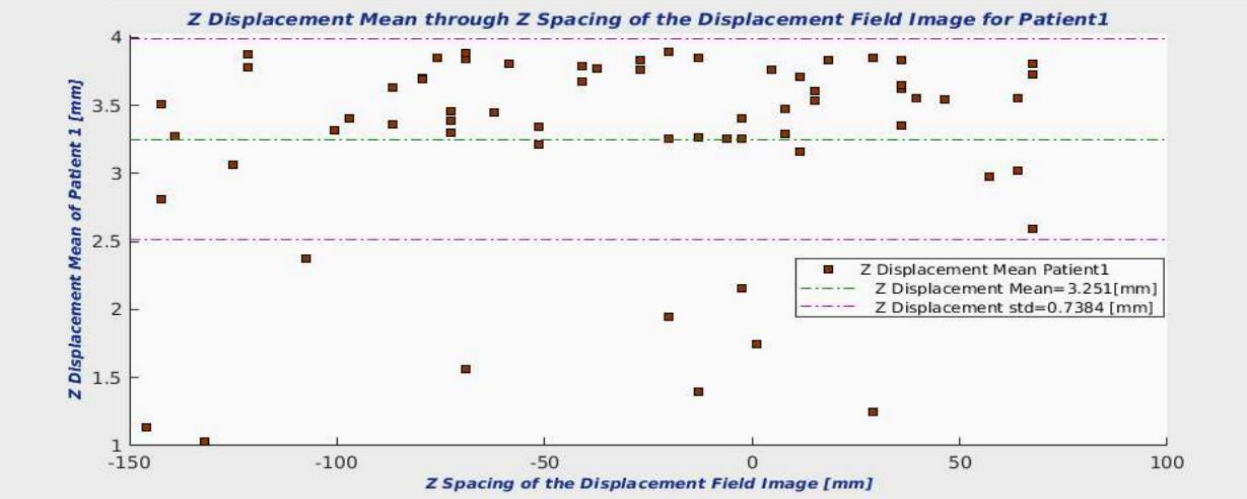

(Figure 2.3.1.13) ΔZ Displacement Mean and Z Spacing of the Displacement Field Image

In Figure 3.3.1.13, most of the displacement occurs between 2.5 mm and 4 mm. The mean of Δz displacement is 3.251 mm and the standard deviation is 0.7384 mm. The following table show a summary of the displacement map of this patient.

Patient 1	**Δx Displacement [mm]**	**Δy Displacement [mm]**	**Δz Displacement [mm]**
Mean [mm]	0.4594	1.4818	3.2510
STD [mm]	0.2607	0.6969	0.7384
Max [mm]	0.7856	2.6416	3.8979
Min [mm]	0.1105	0.7116	1.0341

(Table 2.3.1.1) comparison of Δx, Δy, and Δz Displacements for Patient 1

From Table 2.3.1.1, most of the breathing motion of the liver occurred toward the superior/left/posterior. The largest displacement is toward the superior direction with mean of 3.2510 mm.

2.3.2 Modeling the start phase of inhale to the end phase of exhale for Patient 2

Following the same process for patient 1, the start-inhale phase is the reference image and the end-exhale phase is the deformed image. The following image shows the reference image of patient 2 in anterior/inferior/left view.

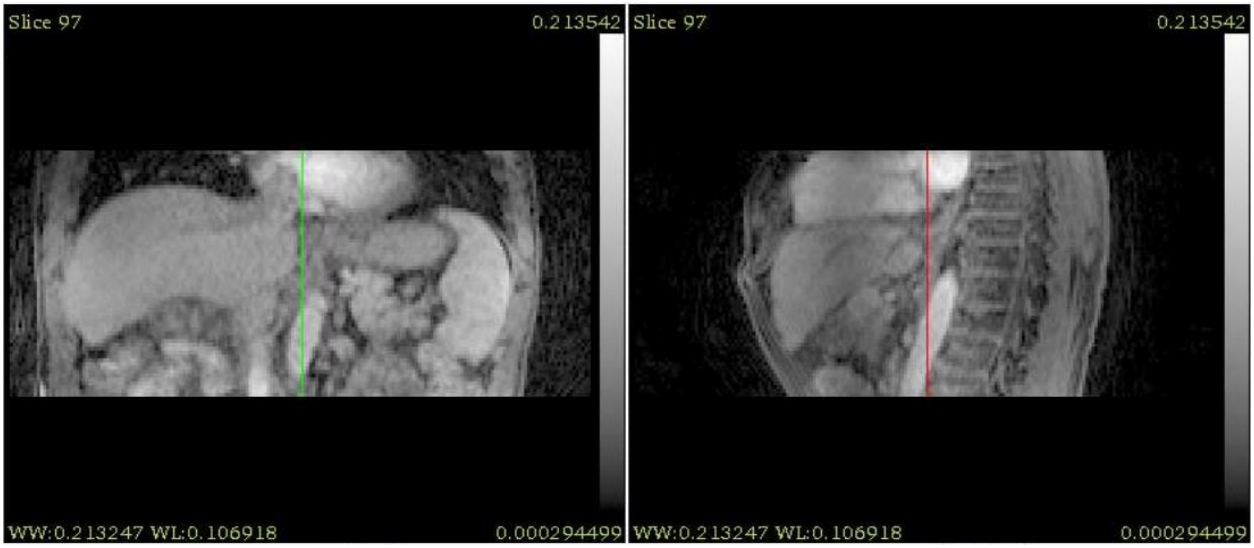

(Figure 2.3.2.1) Reference Image (Inhale Phase)

The moving image is shown below.

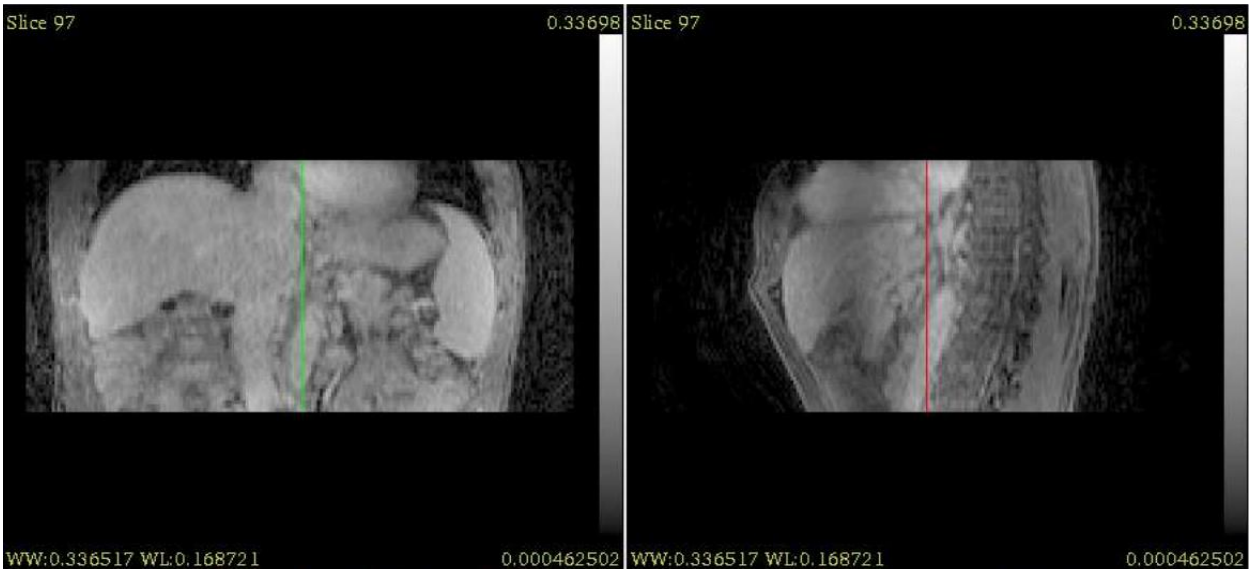

(Figure 2.3.2.2) Floating Image (Exhale Phase)

To determine how much displacement occurred in the liver during breathing, the fast free-form deformation algorithm for non-rigid registration was used as was explained for patient 1.

An array volume of the displacement map after using MATLAB is shown below. The following figure shows the coordinate system of the map.

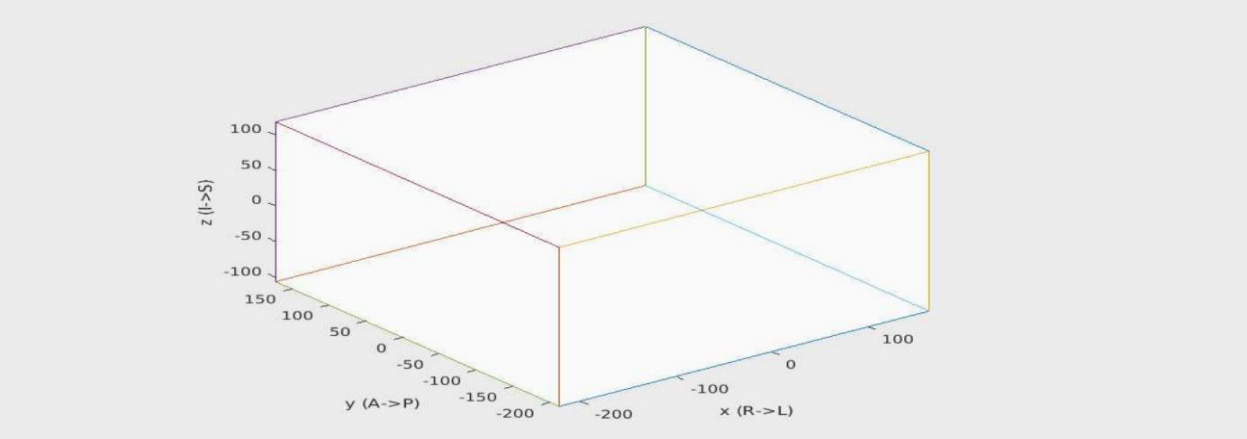

(Figure 2.3.2.3) Volume of the Displacement Map of Patient 2

In Figure 2.3.2.3, Z-axis is superior (+) and inferior (-), X-axis is left (+) and right (-), and Y-axis is posterior (+) and anterior (-).

The histogram of this displacement map is shown below.

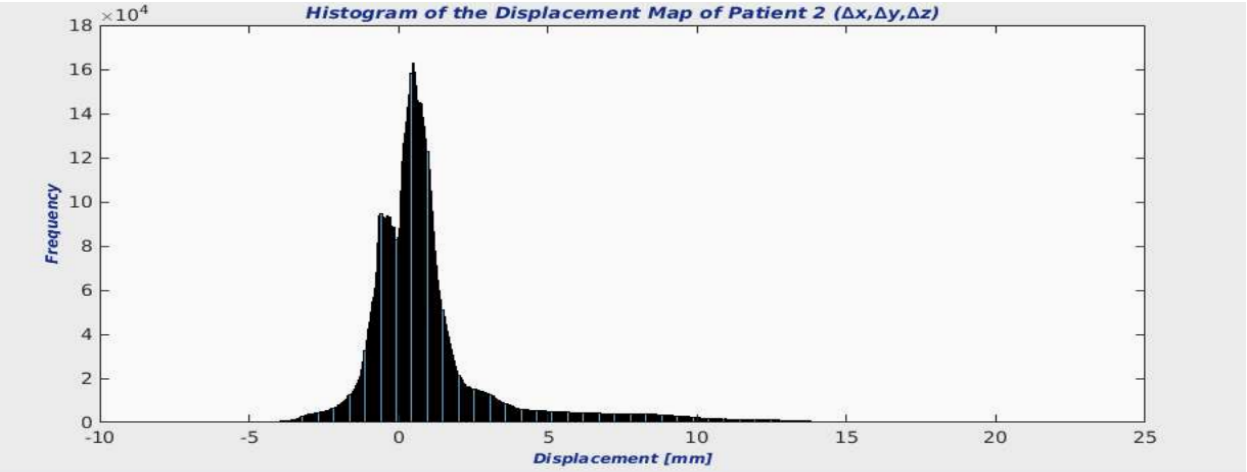

(Figure 2.3.2.4) Patient 2 Displacement Map Histogram

In Figure 2.3.2.4, most of the displacement is approximately between 5 mm and -3 mm. The displacement is more in the positive direction. To figure out the direction in 3D space, this map was separated to study each axis.

The following figure is the Δx displacement map.

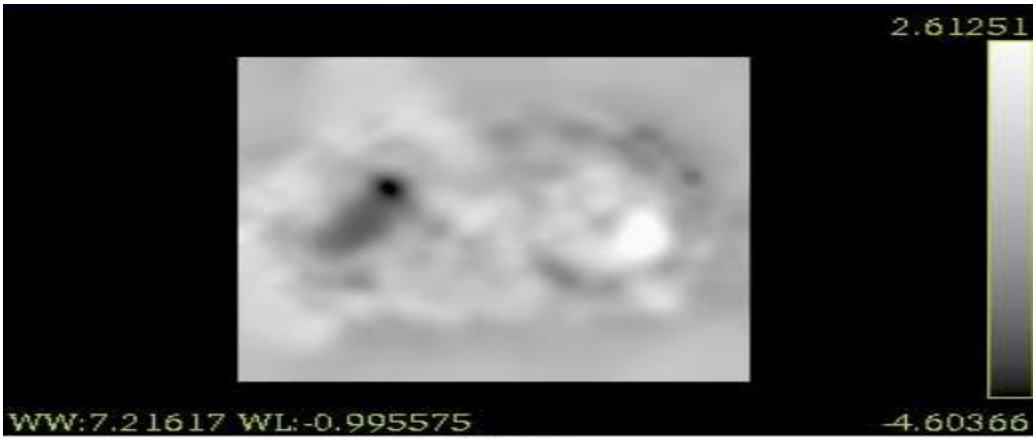

(Figure 2.3.2.5) Patient 2 Displacement Map (Δx)

The Δx displacement map histogram is shown below.

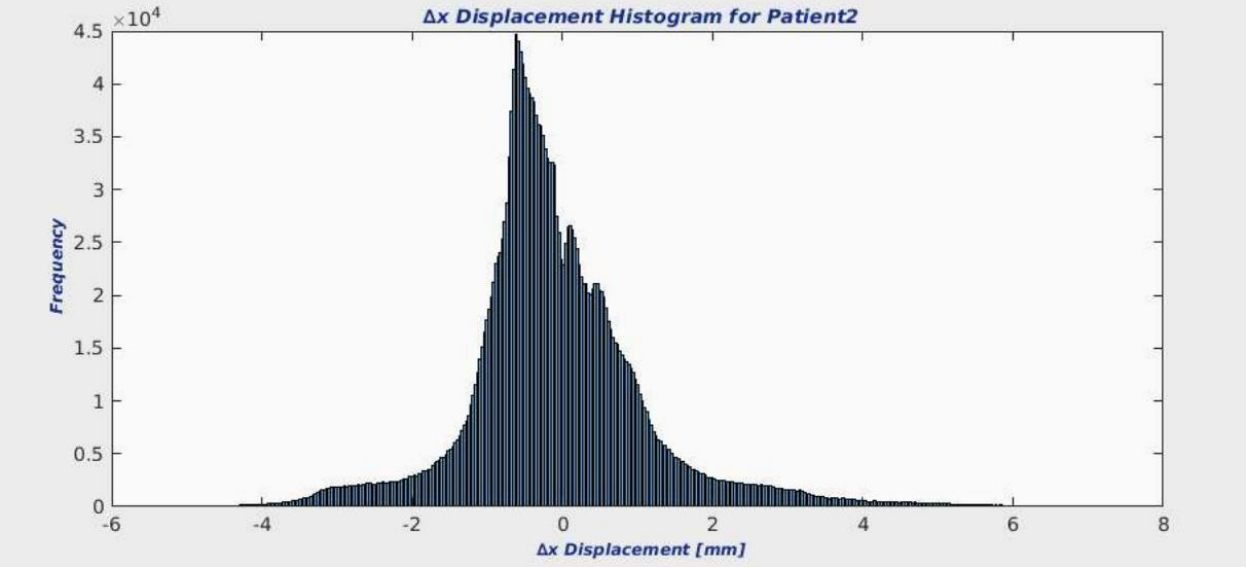

(Figure 2.3.2.6) Patient 2 Δx Displacement Map Histogram

From the above graph, the major displacement occurs approximately between 2 mm and -2 mm, but the frequency is higher in the negative side of the histogram, which means that the displacement is slightly higher in the right direction.

To get the mean and the standard deviation, a graph of the mean of Δx displacement with the left/right direction spacing is shown below.

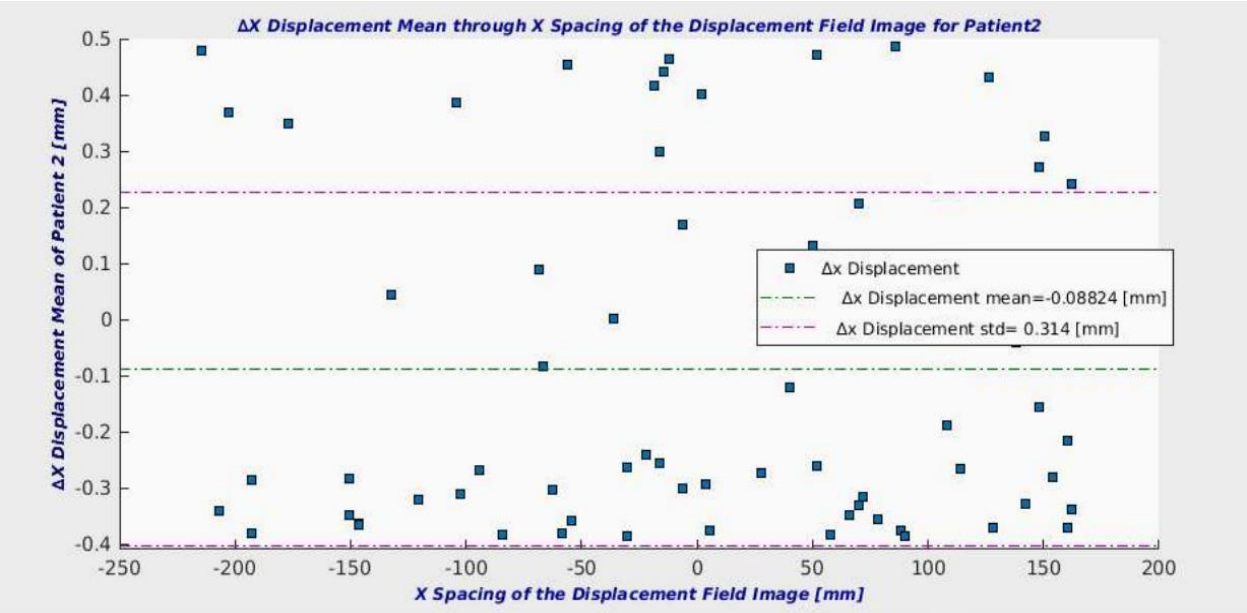

(Figure 2.3.2.7) Δx Displacement Mean and x Spacing of the Displacement Field Image

The mean of Δx displacement is -0.08824 mm and the standard deviation is 0.314 mm. From the mean, the displacement is higher toward the right direction.

The Δy displacement map is shown below.

(Figure 2.3.2.8) Patient 2 Δy Displacement Map

The histogram of this map is shown below.

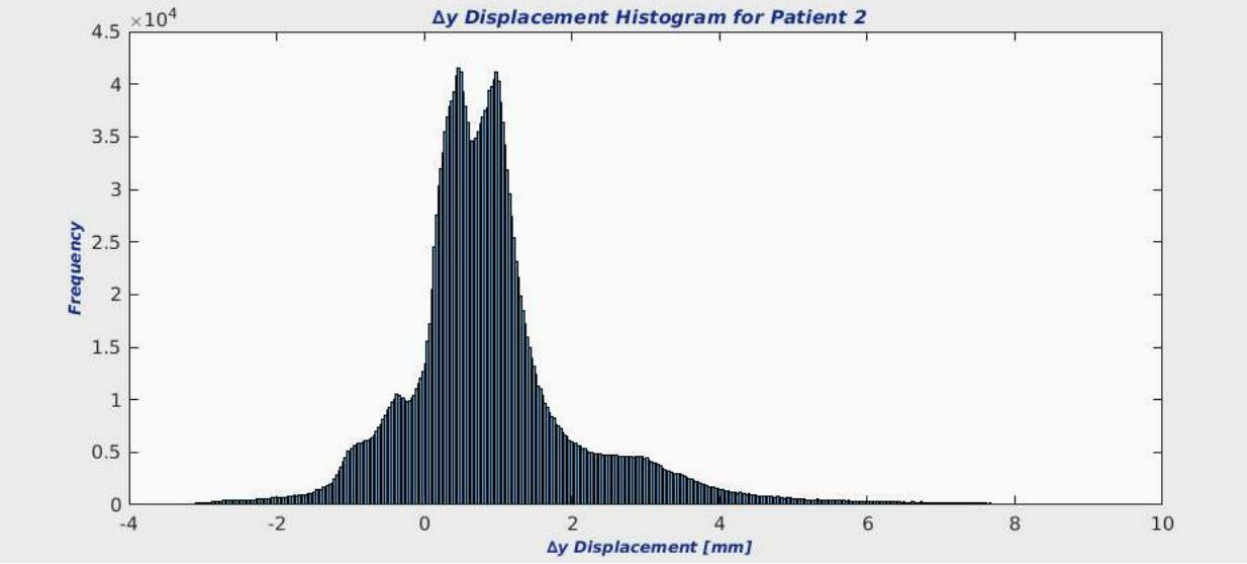

(Figure 2.3.2.9) Patient 2 Δy Displacement Map Histogram

Almost 95% of the displacement occurs approximately between -2 mm and 2 mm and the most frequency is on the positive side of the histogram, which is the posterior direction. The mean and

the standard deviation of Δy displacement is shown in the following graph of Δy displacement with the AP direction.

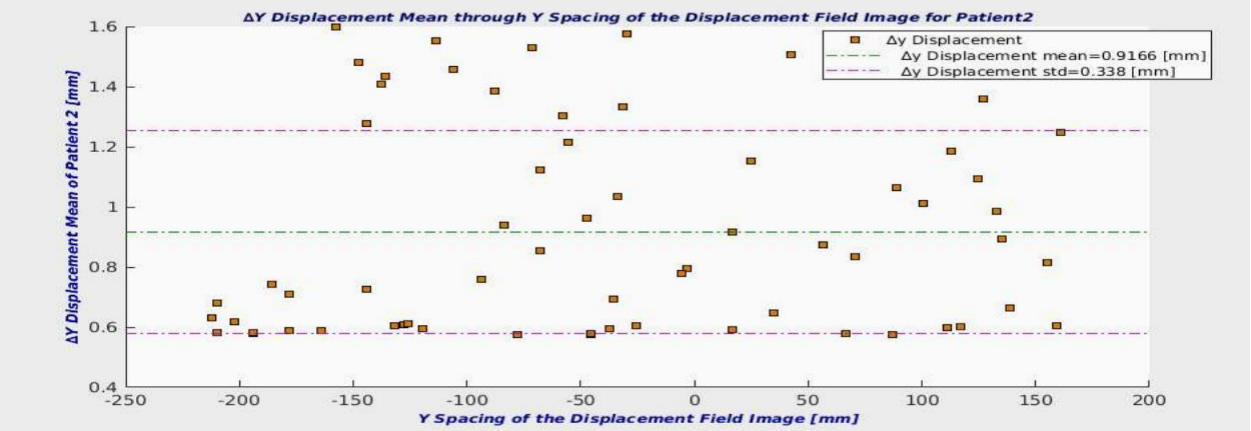

(Figure 2.3.2.10) Δy Displacement Mean and y Spacing of the Displacement Field Image

The mean of Δy displacement is 0.9166 mm and the standard deviation is 0.338 mm. Most of the Δy displacement is toward the posterior direction.

The Δz displacement map is shown below with brightness in the middle.

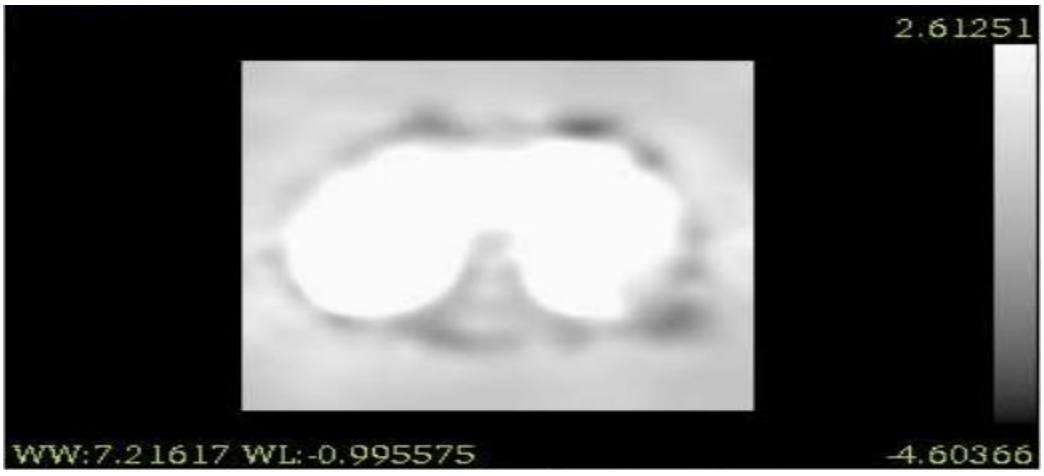

(Figure 2.3.2.11) Patient 2 Δz Displacement Map

The Δz displacement histogram is represented below (Figure 2.3.2.12).

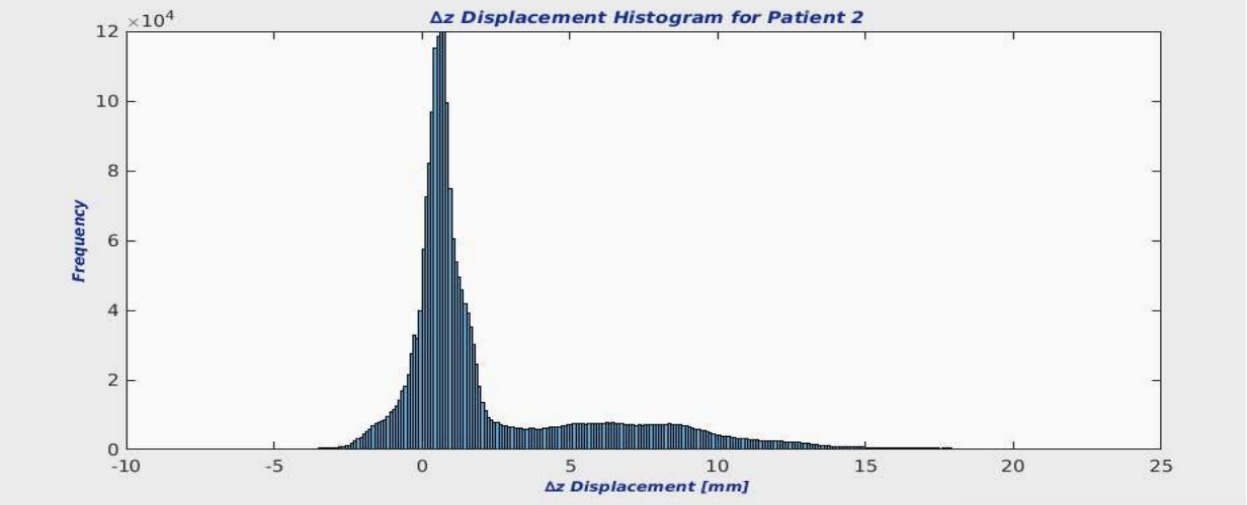

(Figure 2.3.2.12) Patient 2 Δz Displacement Map Histogram

In Figure 2.3.2.12, most of the displacement is approximately between -2 mm and 2 mm. The frequency is very high compared to the Δx and Δy displacements. For calculating the mean and the standard deviation, a graph of the mean of Δz displacement with the SI spacing is shown below.

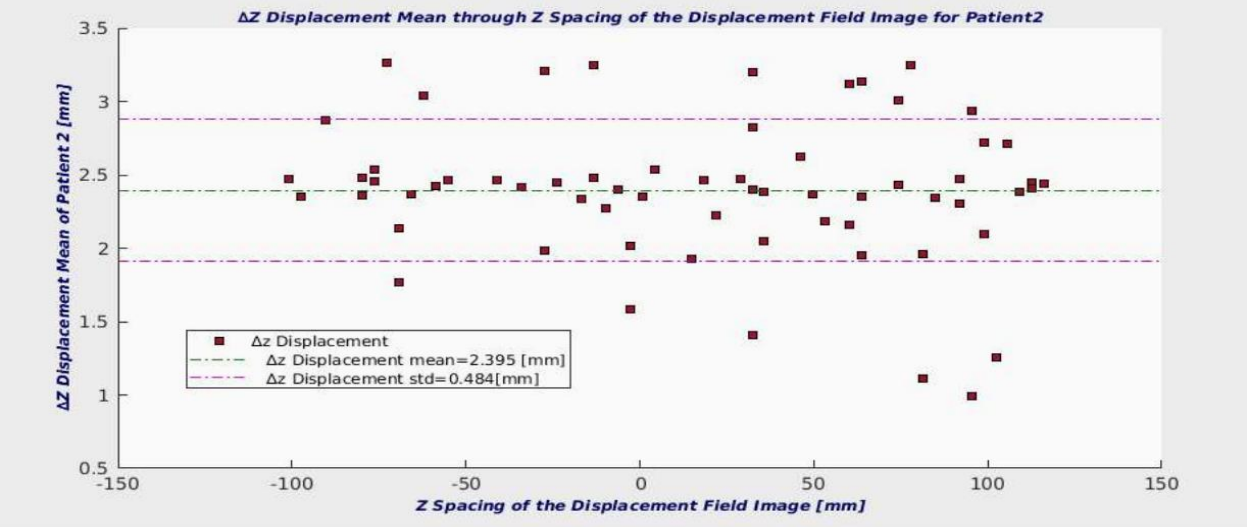

(Figure 2.3.2.13) Δz Displacement Mean and z Spacing of the Displacement Field Image

In Figure 3.3.2.13, the Δz displacement mean is 2.395 mm and the standard deviation is 0.484 mm. Δz displacement is toward the superior direction.

Table 2.3.2.1 shows a summary of the displacements field maps for patient 2.

Patient 2	**Δx Displacement [mm]**	**Δy Displacement [mm]**	**Δz Displacement [mm]**
Mean [mm]	-0.08824	0.9166	2.395
STD [mm]	0.314	0.338	0.484
Max [mm]	0.4869	1.598	3.263
Min [mm]	-0.3844	0.575	0.9891

(Table 2.3.2.1) comparison of Δx, Δy, and Δz Displacements for Patient 2

In short, the displacement of the liver of this patient is toward right/posterior/superior. The largest displacement is toward the SI direction and the smallest is toward the LR direction.

Performing the same process for thirty patients, the following table shows a comparison summary of these thirty patients, displacement fields.

Patient #	Δx Displacement [mm]				Δy Displacement [mm]				Δz Displacement [mm]			
	Mean	Std	Max	Min	Mean	Std	Max	Min	Mean	Std	Max	Min
1	0.4594	0.2607	0.7856	0.1105	1.4818	0.6969	2.6416	0.7116	3.2510	0.7384	3.8979	1.0341
2	-0.08824	0.314	0.4869	-0.3844	0.9166	0.338	1.598	0.575	2.395	0.484	3.263	0.9891
3	0.0140	0.1389	0.2707	-0.1671	1.3675	0.5484	2.1521	0.5200	2.6215	0.5635	3.6536	1.3692
4	0.0234	0.112	0.1707	-0.1505	0.8107	0.1564	1.2088	0.6249	1.4343	0.2476	1.8490	0.7890
5	0.1434	0.0495	0.2043	0.0440	1.4007	0.7969	2.6705	0.1730	3.6751	0.4096	4.2489	2.7643
6	-0.5202	0.1182	-0.2777	-0.6936	1.1308	0.4922	1.9416	0.3093	2.2108	0.4089	2.6769	1.2554
7	0.2027	0.1399	0.4102	0.0070	0.9308	0.2556	1.3752	0.5287	1.6526	0.4892	2.2832	0.5877
8	-0.1975	0.1250	0.0250	-0.3922	1.0929	0.3950	1.6777	0.4527	3.1025	0.5264	3.7149	1.6205
9	0.1942	0.0683	0.2683	0.0774	0.7432	0.2229	1.3128	0.5554	3.0786	0.5762	3.9655	1.4585
10	-0.1264	0.1788	0.1309	-0.3329	1.5840	0.3386	2.0393	1.0921	2.4469	0.5394	3.1546	0.9886
11	-0.5054	0.3296	0.3557	-0.8264	0.2644	0.5818	1.2259	-0.4583	1.9396	0.2407	2.2043	1.1918
12	0.1684	0.1580	0.5979	-0.0594	2.1029	0.7614	3.0218	0.8834	3.1426	0.5252	4.0713	1.8139
13	0.0322	0.3983	0.5998	-0.5549	1.1053	0.6886	2.1359	0.3309	1.5649	0.4403	1.9774	0.3043
14	0.4324	0.1968	0.7637	0.1125	0.7117	0.7104	1.6289	-0.3588	2.7746	0.2683	3.2053	1.9471
15	0.1976	0.0931	0.3316	0.0708	0.6009	0.1305	0.7572	0.3902	2.3941	0.1784	2.5569	1.8155
16	0.1115	0.2347	0.3574	-0.3159	1.0917	0.4011	1.5768	0.5793	3.2763	0.4960	3.9326	1.8139
17	0.3337	0.1925	0.6756	0.0540	1.2750	0.7636	2.5339	0.0939	2.7331	0.7034	3.5602	0.6520

18	0.1423	0.0561	0.2183	0.0095	1.4753	1.2292	3.9029	-0.0281	3.9328	1.0196	4.9029	1.3076
19	0.4130	0.2076	0.6637	0.1190	1.5521	0.8174	2.7652	0.4745	3.4833	0.6569	4.0094	1.7731
20	-0.0566	0.0705	0.0791	-0.1451	0.7303	0.5327	1.3726	-0.1677	1.8224	0.3045	2.1423	1.2329
21	-0.0419	0.2116	0.2013	-0.3902	0.4628	0.3451	0.8550	-0.1062	2.7493	0.4688	3.2560	1.3203
22	0.2102	0.1027	0.3654	0.0477	1.4036	0.3324	1.7997	0.9266	3.1863	0.8098	4.2324	1.4168
23	0.2927	0.0427	0.3673	0.2120	1.1396	0.7425	2.5302	0.1872	1.4458	0.3623	2.2146	0.8105
24	-0.1275	0.0698	-0.0315	-0.2416	0.6752	0.1274	0.8943	0.4877	1.0383	0.2247	1.3664	0.6053
25	-0.1086	0.2488	0.2369	-0.5142	1.1061	0.3808	1.4889	0.2666	1.8312	0.5047	2.8902	1.0771
26	-0.0446	0.1086	0.0833	-0.2770	1.6573	0.5973	2.3528	0.5363	2.4813	0.6811	3.0431	0.4025
27	-0.0863	0.1538	0.1230	-0.3382	1.2746	0.0651	1.3559	1.1415	1.8023	0.5246	2.7273	0.5298
28	0.1886	0.0762	0.3246	0.0472	1.4299	0.3063	1.7651	0.7618	2.5644	0.5125	3.3666	1.2905
29	0.0189	0.2326	0.3926	-0.2746	1.1504	0.4920	2.0240	0.4219	2.1218	0.3433	2.5619	1.2549
30	-0.0065	0.0715	0.0716	-0.1533	0.9372	0.1474	1.1268	0.6773	1.3816	0.2078	1.7971	1.0664

(Table 2.3.2.2) Summary of Δx, Δy, and Δz Displacements for 30 Patients

From table. 2.3.2.2, we can conclude that the maximum displacement is toward the SI direction for all thirty. The motion of the liver during breathing varies from one patient to another. The liver of some patients during breathing moves toward the right/posterior/superior and for others moves toward left/posterior/superior.

The following figure shows the mean of Δx displacement for 30 patients.

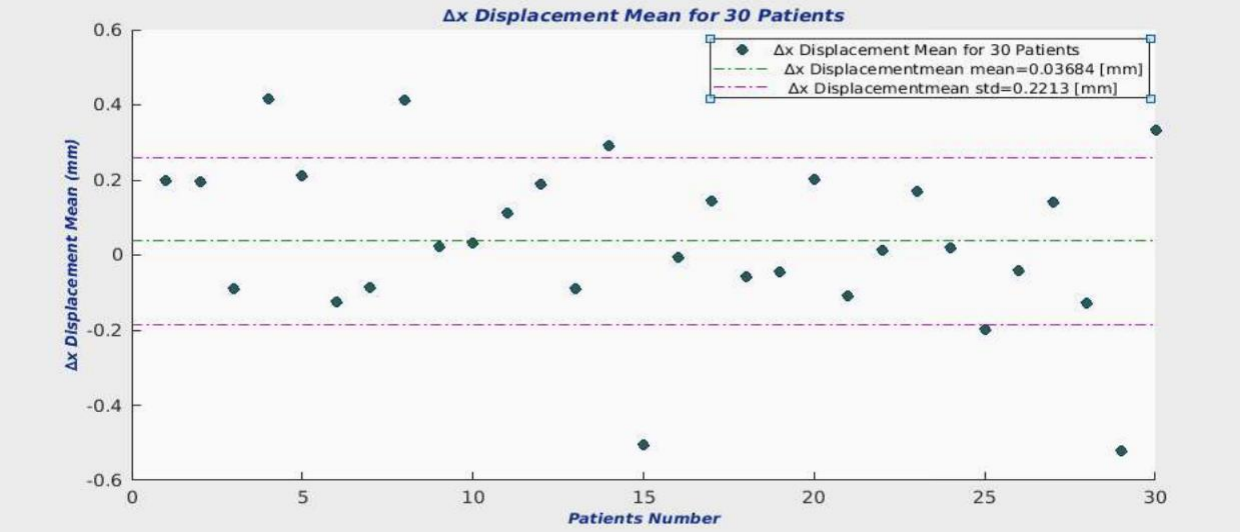

(Figure 2.3.2.14) Δx Displacement Mean for 30 Patients

In short, the mean of Δx displacement for 30 patients is 0.03684 mm and the standard deviation is 0.2213 mm. These results show that the displacement through the LR direction is quite small in the left direction.

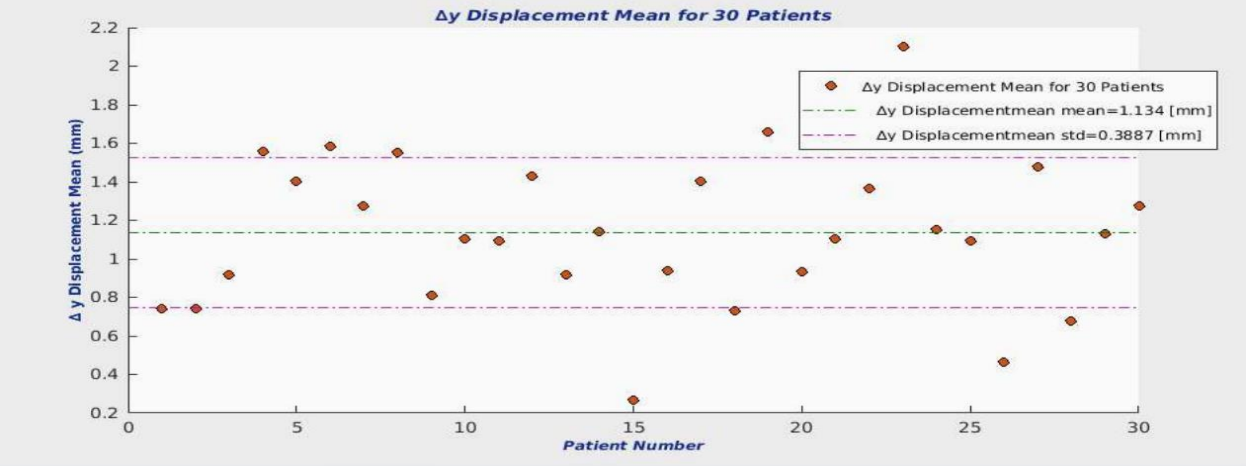

(Figure 2.3.2.15) Δy Displacement Mean for 30 Patients

In Figure 2.3.2.15, the mean of the Δy displacement for 30 patients is 1.134 mm and the standard deviation is 0.3887 mm. More displacement is toward the posterior direction other than the anterior direction.

The Δz displacement mean for the 30 patients is calculated in the following Figure

(Figure 2.3.2.16) Δz Displacement Mean for 30 Patients

From the above graph, the mean of the Δz displacement is 2.438 mm and the standard deviation is 0.755 mm. More displacement is toward the superior direction of the z axis (SI). The following graphs show the Δx, Δy, and Δz displacements' standard deviation for 30 patients. The first graph is the Δx displacement standard deviation for each patient with the patient number.

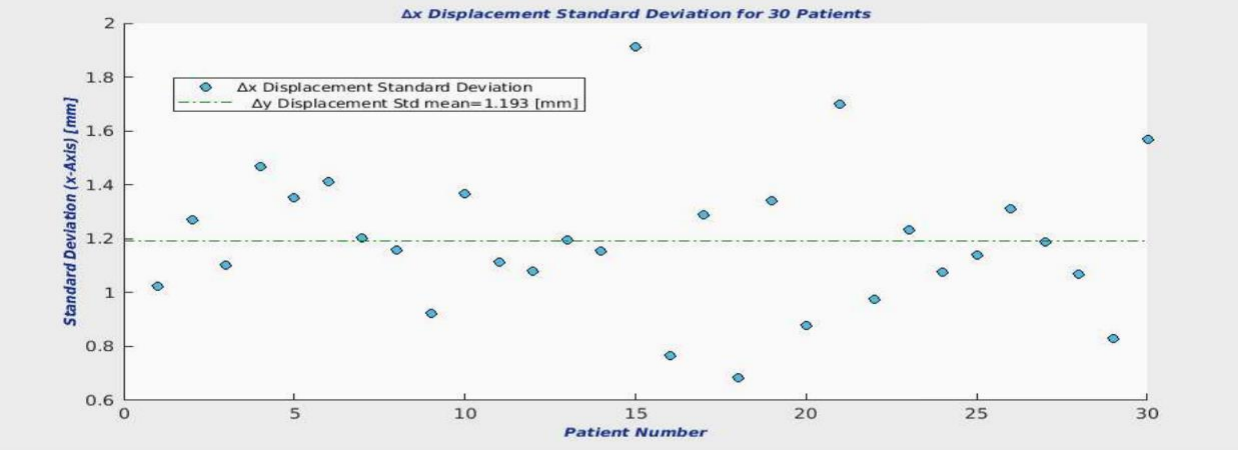

(Figure 2.3.2.17) Δx Displacement Standard Deviation for 30 Patients

The second graph is the Δy displacement standard deviation for each patient with the patient number.

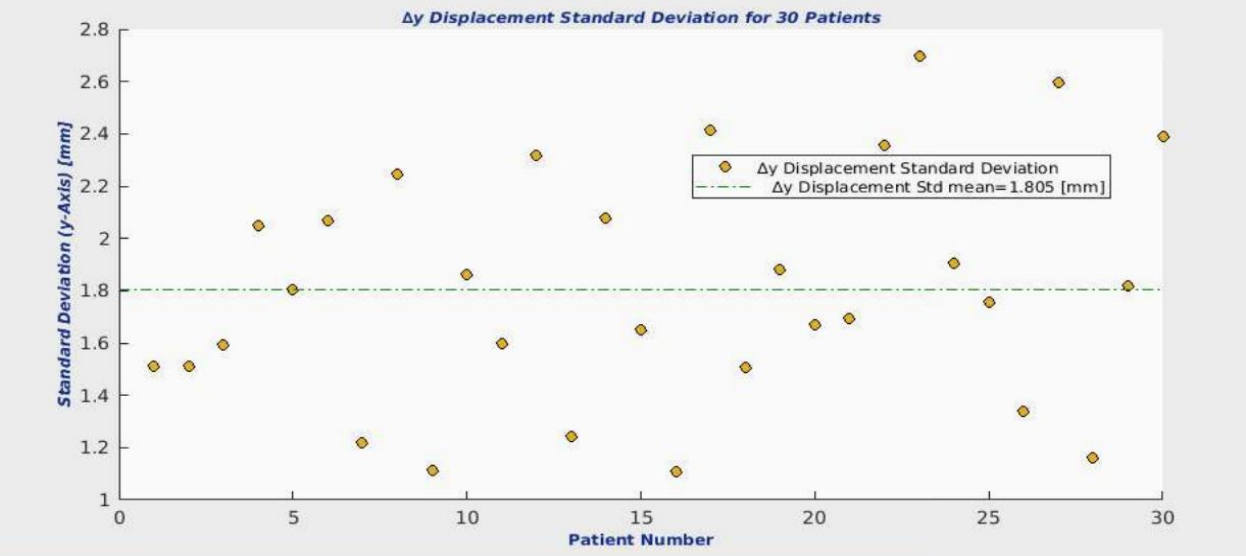

(Figure 2.3.2.18) Δy Displacement Standard Deviation for 30 Patients

The third graph is the Δz displacement standard deviation for each patient with patient number.

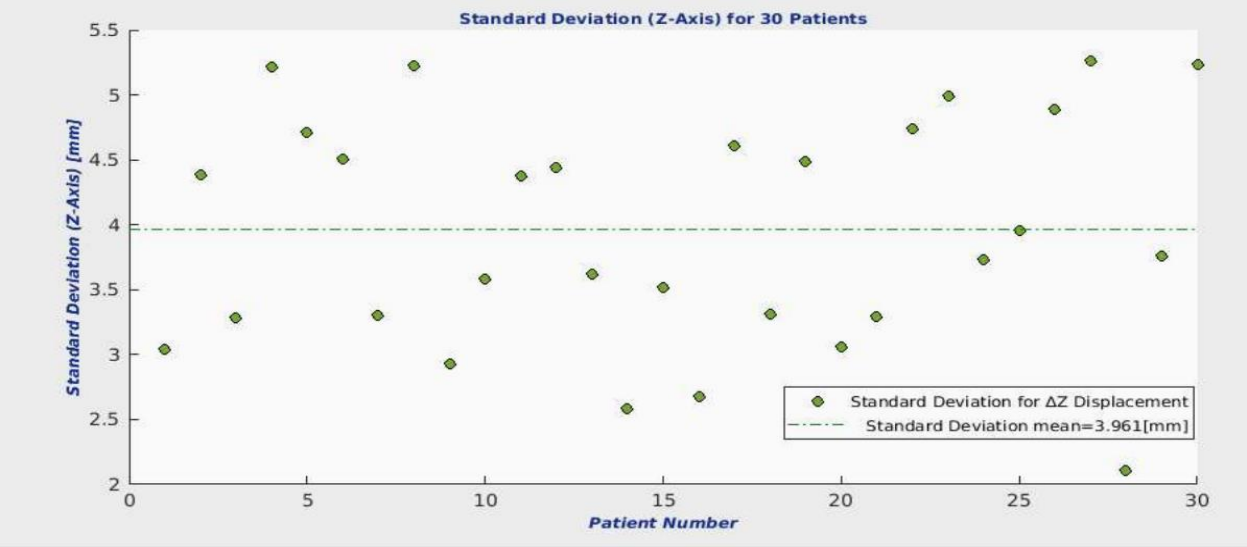

(Figure 2.3.2.19) Δz Displacement Standard Deviation for 30 Patients

2.4 Conclusion

We have performed a non-rigid registration using the fast free-form deformation algorithm for non-rigid registration between the start-inhale phase and the end-exhale phase for each patient for thirty patients. We conducted an analysis of the displacement map for each patient, and we found that the maximum displacement occurs in the SI direction. The AP displacement is high compared to the LR displacement. The mean of the Δx displacement is 0.03684 mm and the standard deviation is 0.2213 mm. Moreover, the Δy displacement mean is 1.134 mm and the standard deviation is 0.3887 mm. The highest displacement is through SI, with a mean of 2.438 mm and standard deviation of 0.7511 mm. These results are from the modeling of the inhale to exhale for the individual patients, and we assume that these results are valid for building the mean population model.

CHAPTER 3

Population Mean Liver Model

3.1 Introduction

Breathing motion of the liver requires a fair amount of research, starting with the individual patient and then across patient population. Quantifying breathing motion first registers baseline shifts of the liver with respect to the surrounding bony anatomy. Because of the daily change of liver position during the treatment fractions, it is necessary to localize the reference breathing motion of the liver in the treatment session and find to the corresponding reference of the breathing motion at planning to avoid errors during the delivery of the dose. Image registration helps to solve this issue. Non-rigid registration is the most suitable method for breathing motion. Deformable image registration (DIR) has been extensively studied over the past two decades due to its essential role in many image-guided interventions (IGI). IGI demands a highly accurate registration that maintains its accuracy across the entire region of interest. This work shows an implementation of a biomechanically based platform, MORFEUS which is used to build a mean population model of the liver. MORFEUS is discussed in section 3.4.

3.2 Method

MRI images of 30 liver cancer patients were used. Starting with the preprocessing step, we started with manually drawing the ROI on the end - exhale phase for each patient for thirty patients using imFIAT (a software to show images and their analysis). For each patient, there were 64 slices for the end - exhale phase. Then, these images are used as DICOM RT structures (a kind of images that used in clinical purposes) to make sure that the MORFUES and Hypermesh could run it. Hypermesh is discussed in section 3.3. Figure 3.3.1 shows a manual liver ROI drawing on a cross - sectional plan for the reference patient. We chose the largest liver with the best look at the liver across the thirty patients to be the reference liver. After that, we performed the registration using MORFEUS, which was discussed in detail in the discussion section. This algorithm helped to get the final registration, and then mathematical methods are applied to get the mean population displacement, which is the final model.

3.3 Discussion

The following images show several patients with manual liver ROI. The first image is the reference patient image.

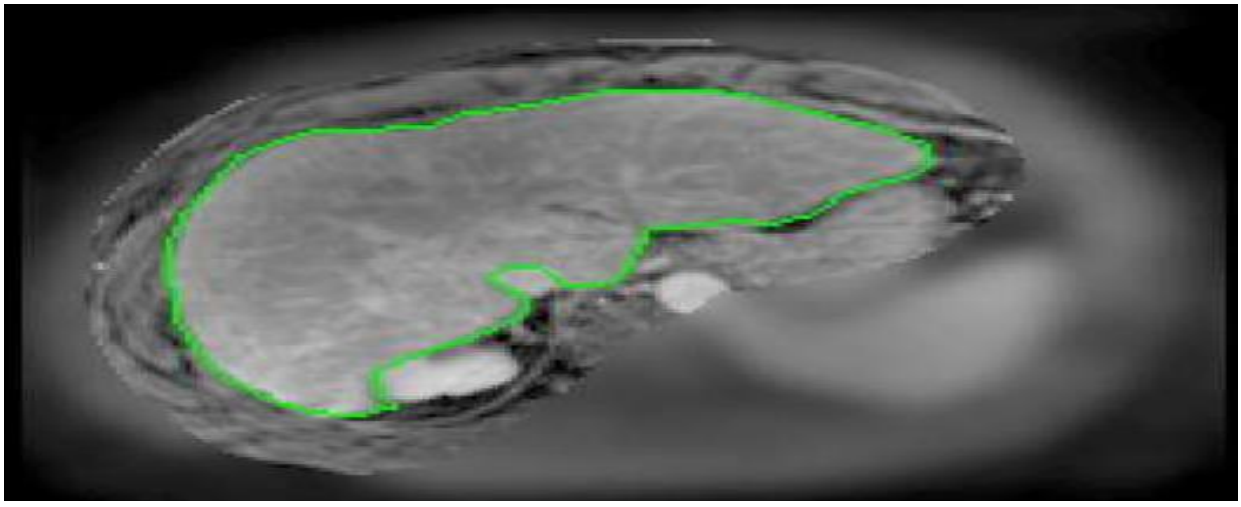

(Figure 3.3.1) Reference Patient with Liver ROI

Across all the patients' data that are used in this study, the liver shape is totally different from patient to another. The following images show how much different there is between the shape of the liver for these two patients.

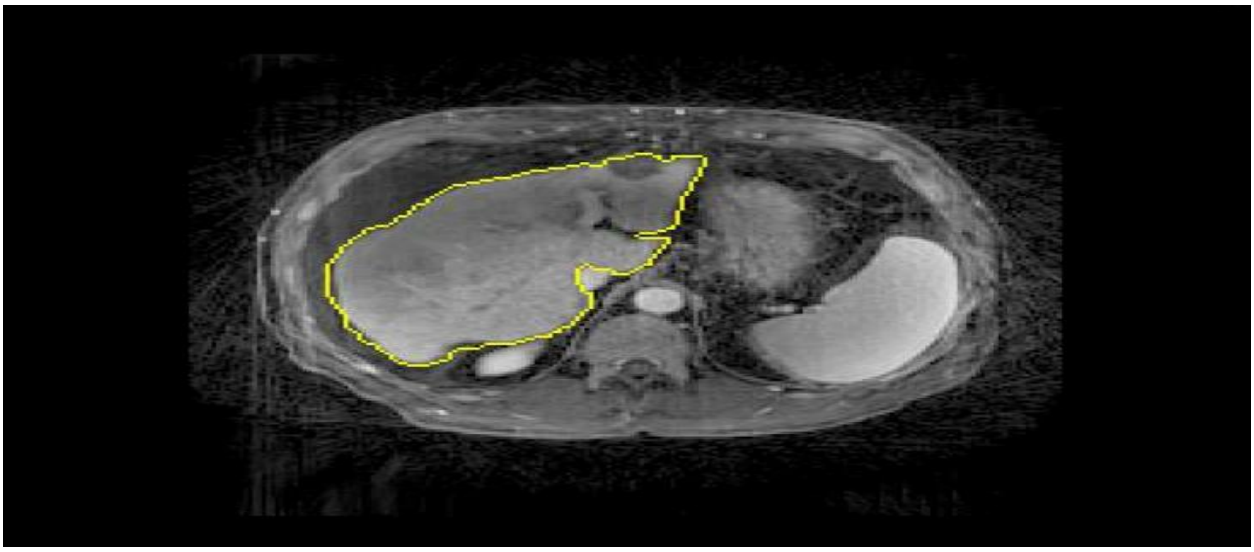

(Figure 3.3.2) Liver ROI for Patient 2

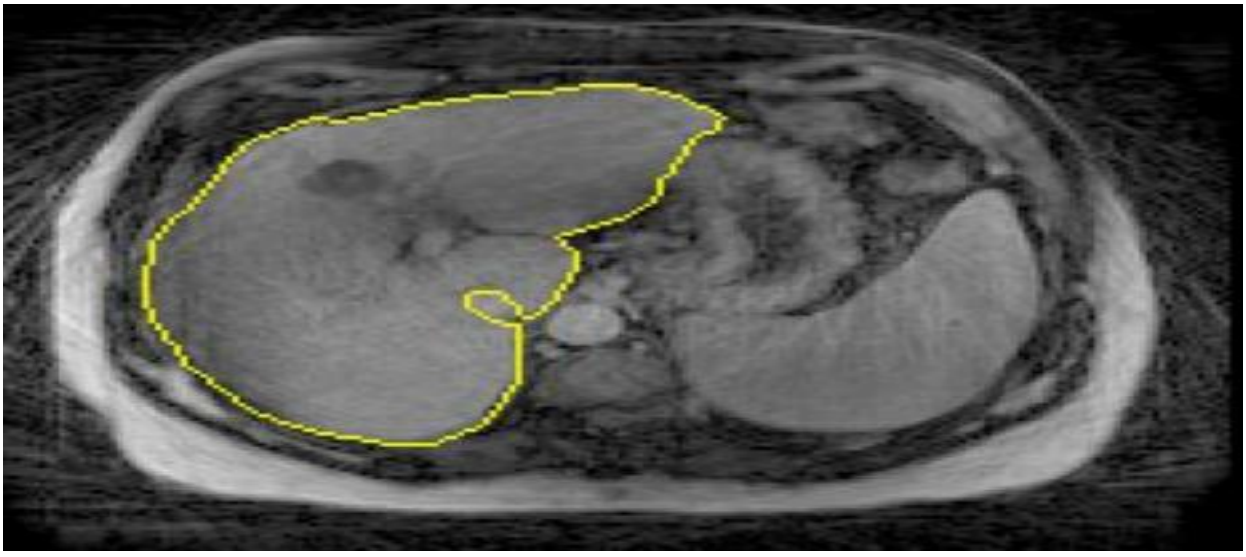

(Figure 3.3.3) Liver ROI for Patient 3

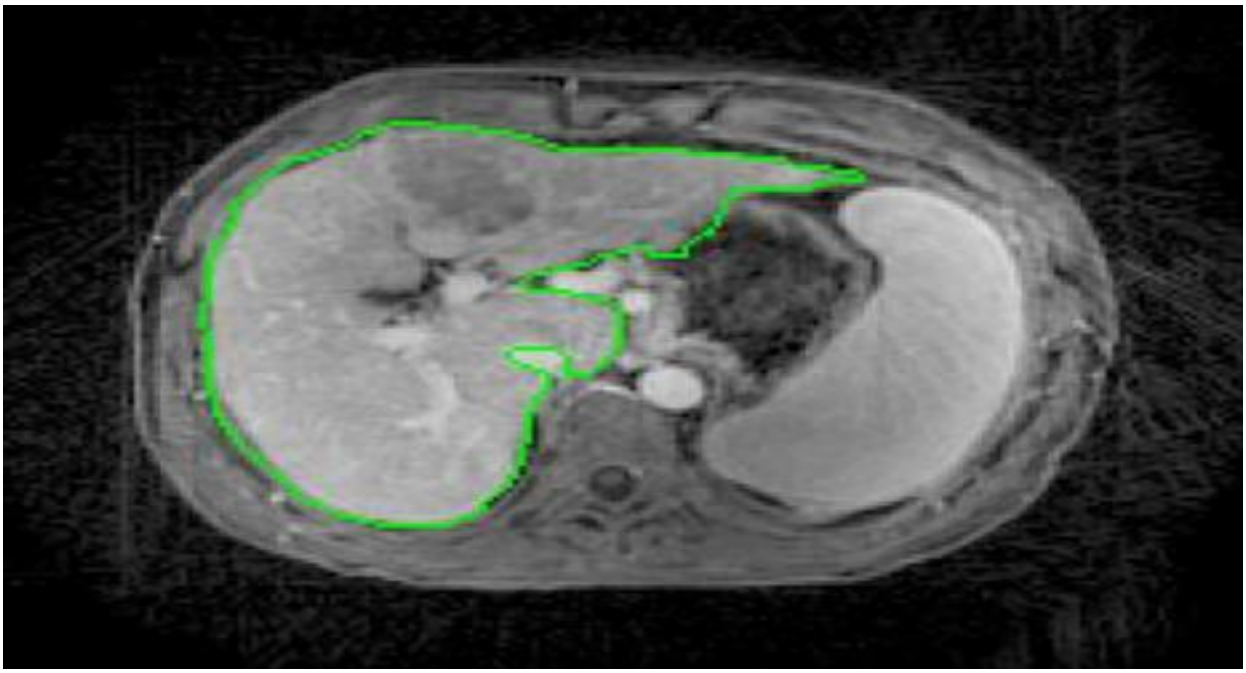

(Figure 3.3.4) Liver ROI for Patient 4

The next step is to apply MORFEUS. The purpose of applying MORFEUS is to allow reduction of data keeping all the information intact. MORFEUS integrates commercially available FEM pre- and post-processes (HYPERMESH v7.0, Altair Engineering, Troy, MI), finite element analysis (FEA) software packages (ABAQUS, ABAQUS Inc., Pawtucket, RI), and the treatment planning system. MORFUES [2] has two input images. One is the reference liver ROI image and the other one is the floating liver ROI image. ROI is converted into triangular Mesh. The binary image data is down sampled from 256x256xN to 64x64xN. This down sampled data is converted to triangular mesh by using Laplacian smoothing to improve the appearance without changing topology. Laplacian smoothing is performed in 50 iterations. The surface is then reduced by using decimation function. Combining Laplacian smoothing and mesh decimation allows reduction of data, keeping all the information intact. The triangular mesh is then imported to FEM preprocessor, which consist of a series of nodes connected to form tetrahedrons and save them as STL files. These tetrahedrons describe the entire volume of the liver. The purpose of FEM is to create interior

surface mesh of a liver without internal organs. The FEM model has ability to describe biomechanical materials using simple and complex models. In performing image deformation, base model is selected that is deformed into all other representation. The exhale data set is used as base model in this study. Then, a rigid registration is initially performed using a chamfer registration. After rigid registration, a demons registration is performed, which provides a surface projection of the two FEMs and provide boundary constraints relating the surface of the liver between the two patients' exhale phase, which is then applied to the FEMs. The output of this algorithm is un-deformed nodes with the deformed nodes and how much the displacements of the nodes are. Every patient was deformed to the reference patient. The following schematic diagram shows the implementation of deformed patient two to the reference patient using MORFEUS.

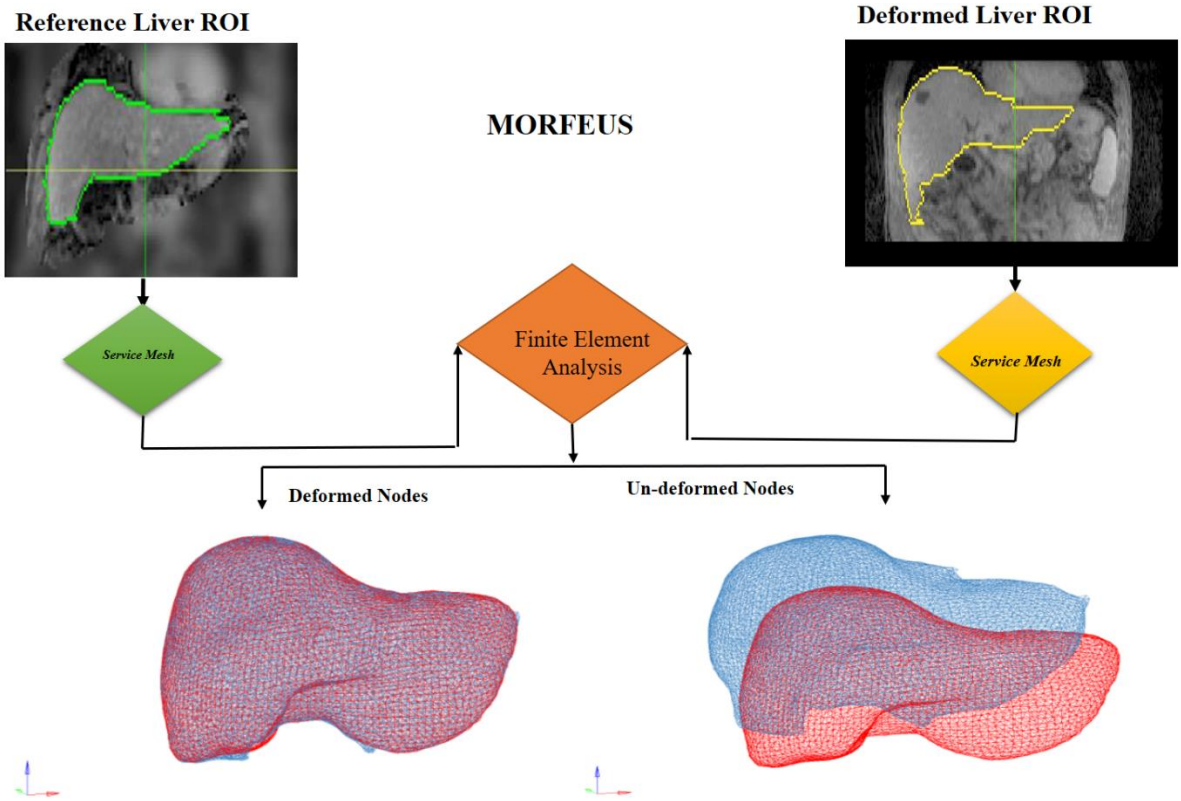

(Figure 3.3.5) Schematic Diagram of Implementation of MORFEUS

The output of this algorithm is thousands of un-deformed and deformed nodes. For each patient, we got different numbers of nodes, which means that the shape of liver changes from patient to patient. The following table shows MORFEUS un-deformed and deformed nodes for 30 patients.

Patients Number	Un Deformed Nodes	Deformed Nodes
1	12860	12860
2	12860	12860
3	8563	8563
4	9066	9066
5	12043	12043
6	12843	12843
7	6516	6516
8	7982	7982
9	9844	9844
10	9810	9810
11	12559	12559
12	9280	9280
13	9692	9692
14	13213	13213
15	9502	9502
16	13599	13599
17	13482	13482
18	11006	11006
19	10466	10466
20	8341	8341
21	7469	7469
22	10149	10149
23	11518	11518
24	8139	8139
25	10977	10977
26	9491	9491
27	10327	10327
28	8359	8359
29	8261	8261
30	7969	7969

(Table 3.3.1) MORFEUS Nodes

In addition, MORFEUS aligned the superior and inferior direction perfectly and did not work that much to cover the whole liver through the left/right and posterior/anterior.

For each patient, we have a displacement field map from registering exhale to inhale for each patient and the output result from MORFEUS which contains deformed and un-deformed nodes. We also checked the coordinate system of the Analyze format (nii) of the displacement field images. The coordinate system of these images is in LAS (Left, Anterior, and Superior) orientation. We found also that the DICOM coordinate system is in LPS (Left, Posterior, and Superior) base. From the header file of the displacement field map of each patient, we have the qoffset_x, qoffset_y, and qoffset_z, which is the x, y, and z coordinates of the first voxel in this image from a point in space. The following figure shows a simple representation of the 1st voxel coordinate of the displacement field map image.

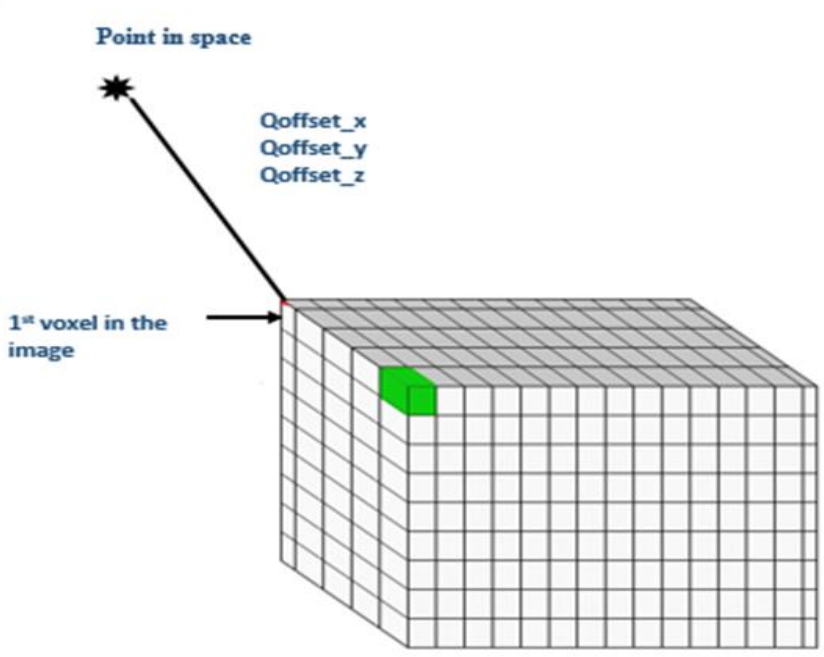

(Figure 3.3.6) Simple Representation of 1st Voxel Coordinate

The following explanation shows how the two displacement images and the nodes from MORFEUS are in the same coordinate system. The first reason to provide this explanation is to make sure that the un-deformed nodes from MORFEUS align inside the same patient displacement field map array volume. For this test, the un-deformed nodes were uploaded inside the volume of the displacement field image using MATLAB.

For patient 2, we got the following result:

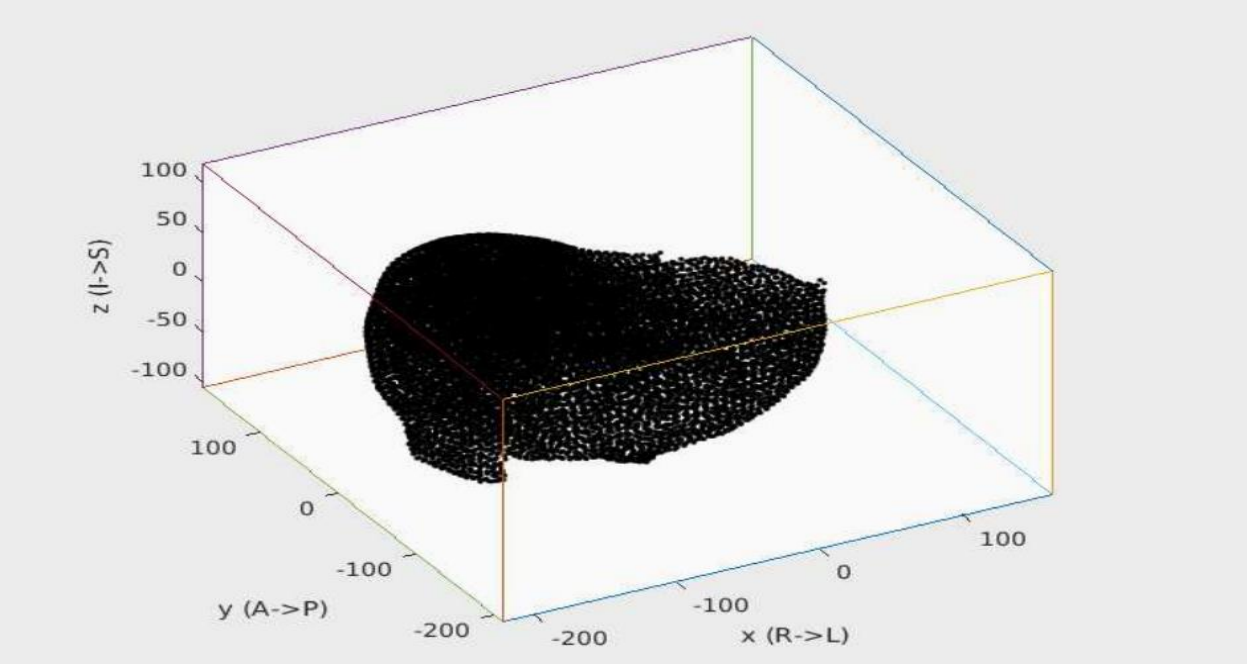

(Figure 3.3.7) Patient 2 MORFEUS Un-Deformed Nodes inside the Displacement Field Map of Exhale to Inhale for Patient 2

The un-deformed nodes align inside the displacement field map image volume. Z axis is positive through the superior and negative through the inferior. Y axis is posterior (+y) and anterior (-y). X axis is left (+x) and right (+x).

The following images show the results of this method for different patients and how the liver orientation is different for each patient.

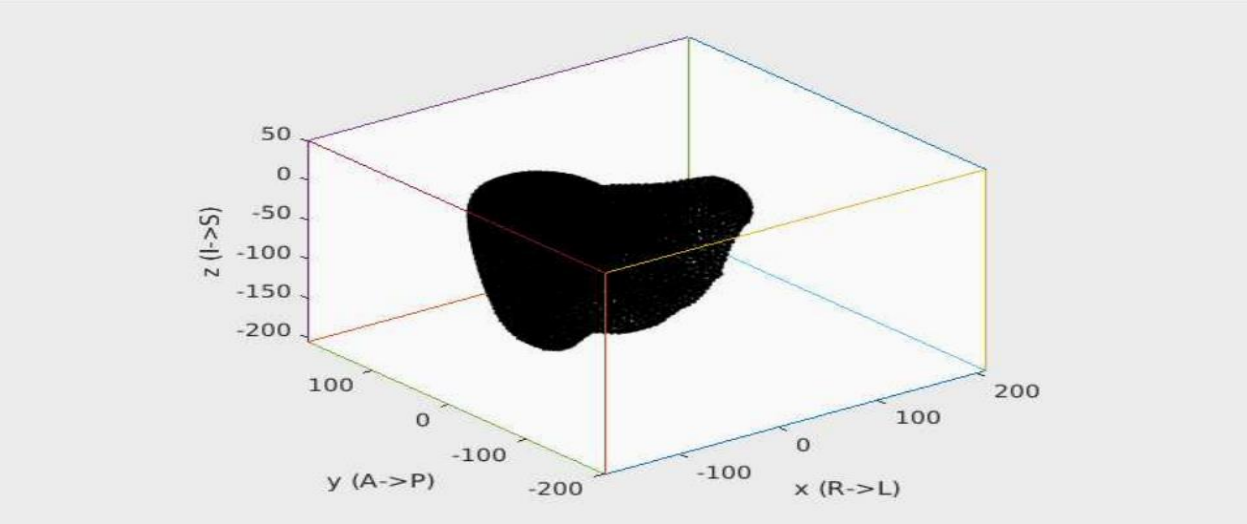

(Figure 3.3.8) Patient 3 MORFEUS Un-Deformed Nodes inside the Displacement Field Map of Exhale to Inhale for Patient 3

Patient 3 has a different orientation from patient 2. This is a really challenging task when creating the population model.

The following image is for patient 4 with a different orientation.

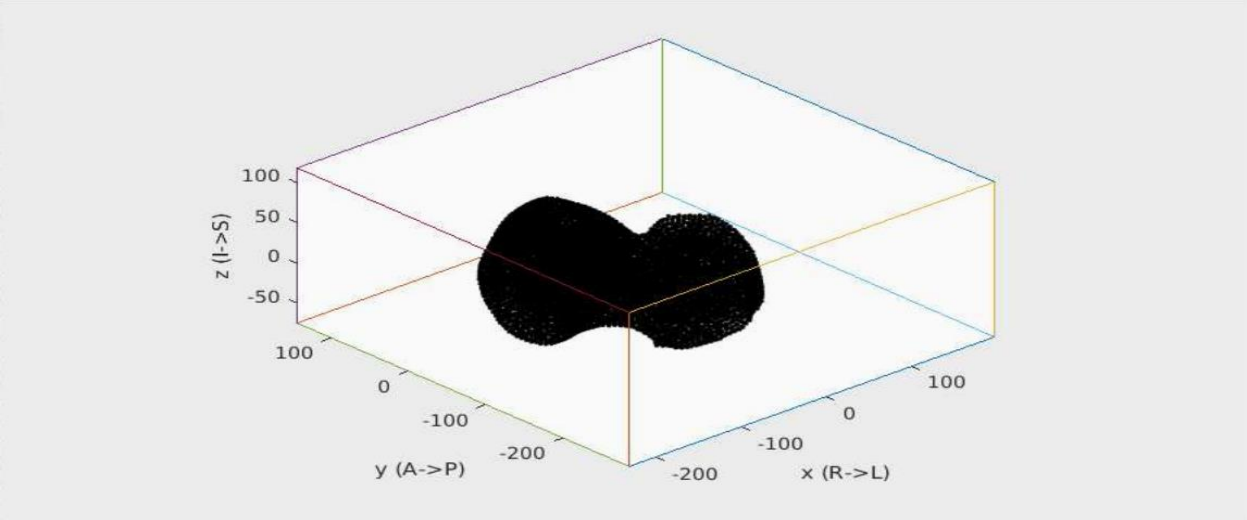

(Figure 3.3.9) Patient 4 MORFEUS Un-Deformed Nodes inside the Displacement Field map of Exhale to Inhale for Patient 4

It can be noticed that the shape of the liver for patient 4 is totally different from the shape of the liver of patients 2 and 3.

The following discussion explains two tests to ensure that these data have the same coordinate system. For patient 7, the liver is really small compared to other patients. The shape of the liver for this patient is shown below.

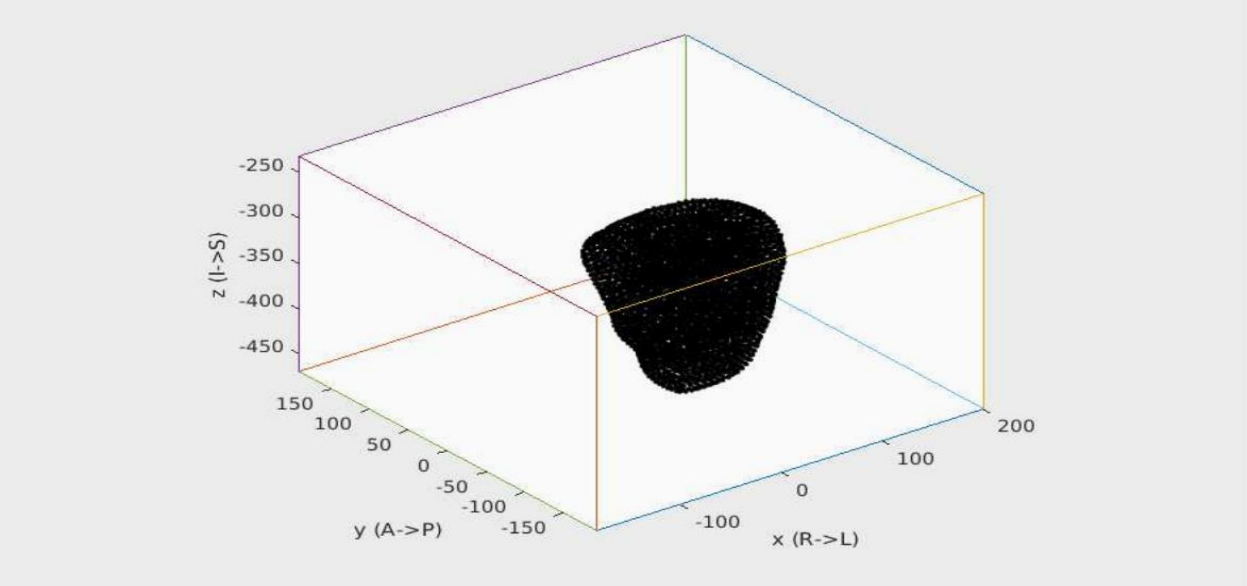

(Figure 3.3.10) Patient 7 MORFEUS Un-Deformed Nodes inside the Displacement Field map of Exhale to Inhale for Patient 7

The following images represent the livers of some patients align inside the displacement field map for each patient. It can be observed that the shape of the livers for each patient is totally different and it can be noted that the orientation of the liver for each patient is variant. In addition, MORFEUS un-deformed nodes that resulted from deformed patient 8 liver to the reference patient liver are aligned totally inside the displacement field map of inhale to exhale alignment of the deformed liver image of patient 8. The following image shows a box, which is the displacement field map as an array volume of patient 8 when align start-inhale phase to end-exhale phase. The

black dots inside the box are the un-deformed nodes from MORFEUS when aligning patient 8 to the reference patient. For the displacement field map that resulted from aligning patient 8 exhale to inhale, the whole image of the end-exhale was deformed to the whole image of the start-inhale phase. When we applied MORFEUS to align patient 8 to the reference patient, we did align the ROI liver of patient 8 to the ROI liver of the reference patient. That means that we did align part of the patient 8 liver image to part of the reference patient liver image. The goal now is to observe if the MORFEUS un-deformed nodes relate to patient 8 displacement field map of exhale to inhale registration.

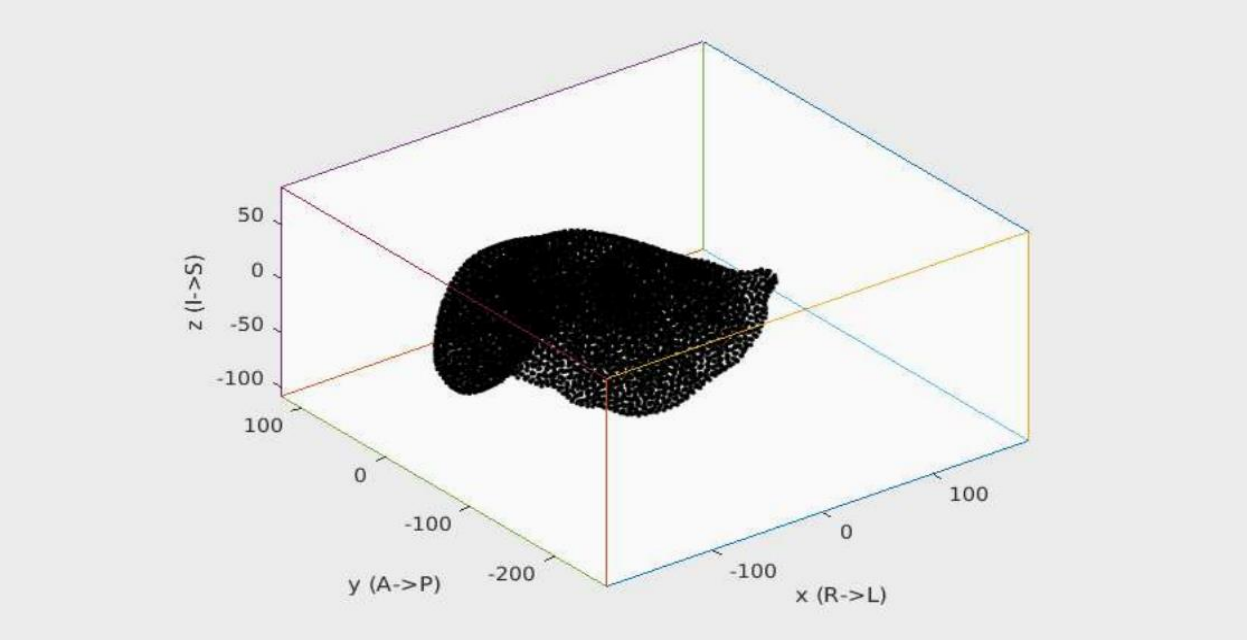

(Figure 3.3.11) Patient 8 MORFEUS Un-Deformed Nodes inside the Displacement Field Map of Exhale to Inhale for Patient 8

The same procedure which was applied to patient 8 liver is now applied on other patients ranging from patient 2 to patient 30. It is observed that the MORFEUS un-deformed nodes of every patient are related to the same deformed patient. In addition, the MORFEUS un-deformed nodes

and the displacement field map of the same patient have the same coordinate system and these nodes are aligned inside the displacement field map.

The following image shows the MORFEUS un-deformed nodes inside the displacement field map of patient 8.

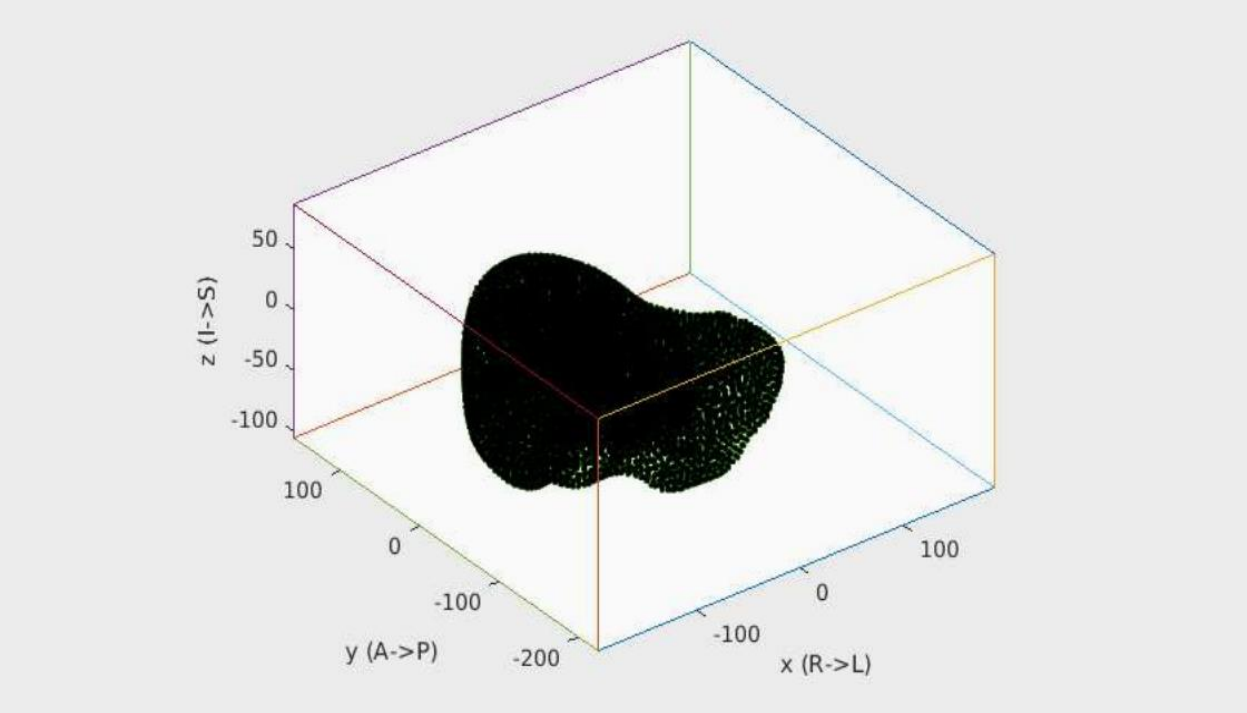

(Figure 3.3.12) Patient 9 MORFEUS Un-Deformed Nodes inside the Displacement Field Map of Exhale to Inhale for Patient 9

The second test is uploading the ROI of the reference patient image and gridding the deformed nodes of any patient to the reference ROI (Figure 3.34), considering that the un-deformed nodes from MORFEUS will align in the floating image and the deformed nodes will align in the reference patient ROI.

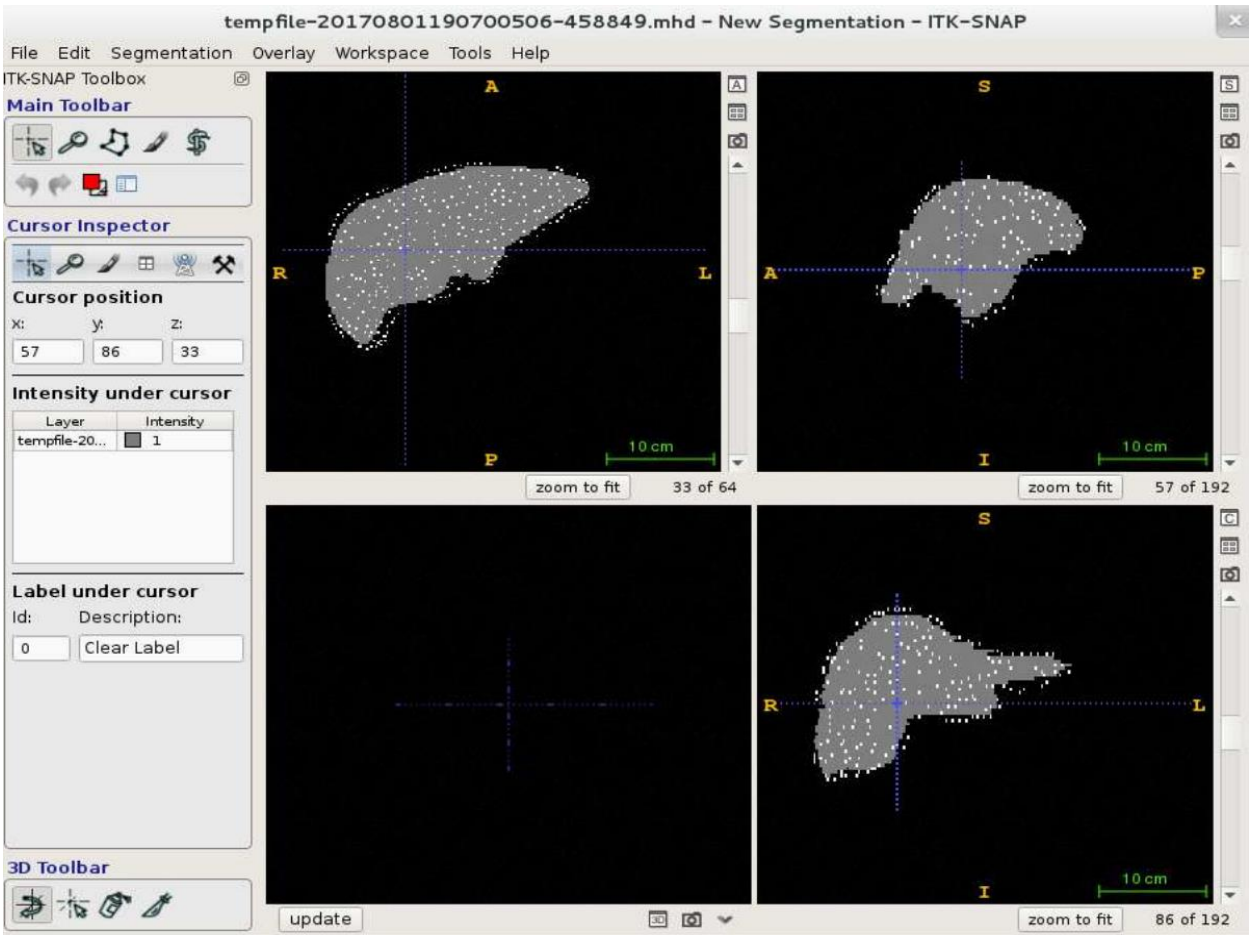

(Figure 3.3.13) Deformed Nodes inside ROI of the Reference Image

Almost all the deformed nodes fall inside the reference liver ROI. Thus, the deformed nodes from MORFEUS relate to the reference patient and the un-deformed nodes relate to the aligned patient. The following image shows the deformed patient liver ROI with un-deformed nodes from MORFEUS.

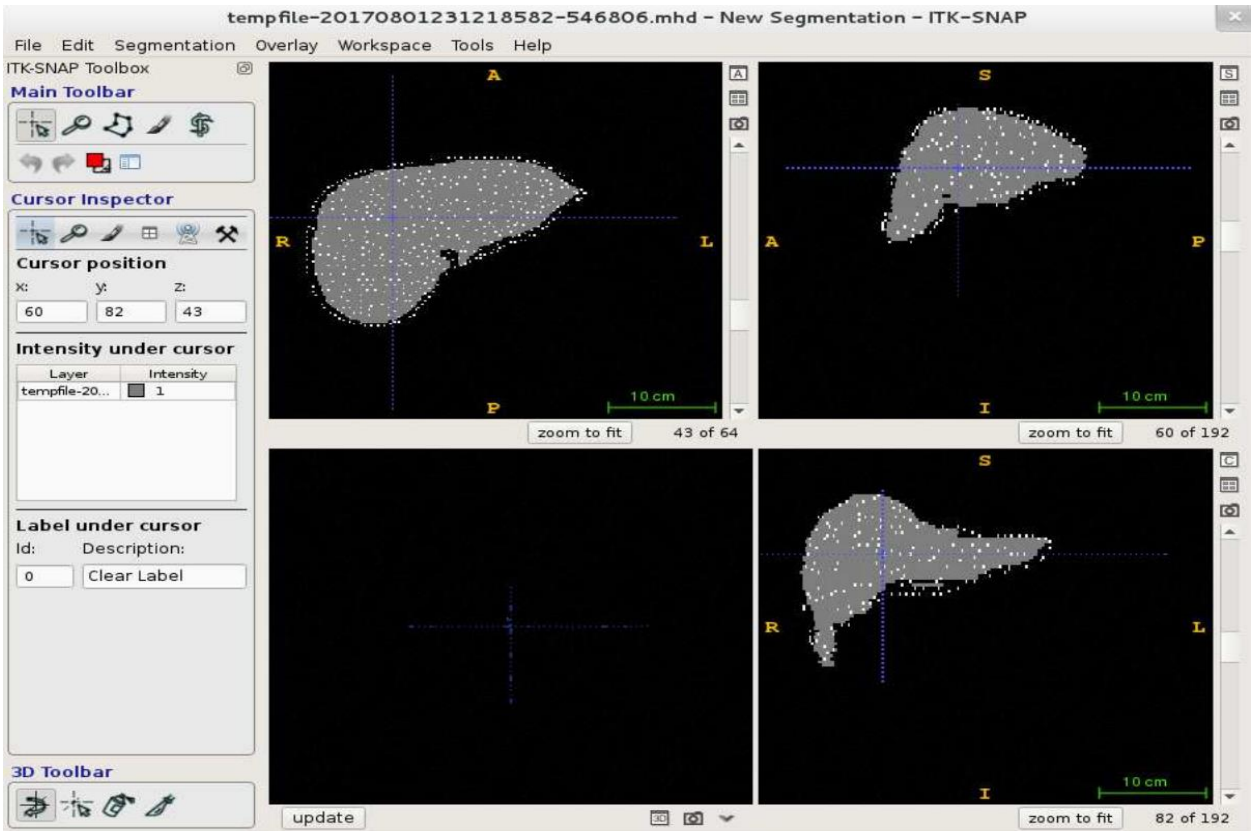

(Figure 3.3.14) Un-deformed Nodes inside ROI of the Reference Image

We have finished the examination of the orientation and coordinate system. Now, the final step is creating the mean population model. We sampled the displacement field map of exhale to inhale for each patient at the location of the Un-deformed MORFEUS nodes for the related patient. After that, we assigned the sampled displacement field to the corresponding deformed MORFEUS nodes. Now, we need to bring all the patients into one 3D space using linear interpolation. After that, we interpolated the combination of sampled displacement fields and the MORFEUS deformed nodes to the voxel coordinate values of the reference patient. This step helped to put all patients into one 3D space with the same orientation. The next step was omitting any part that was outside of the MORFEUS deformed nodes. We also sampled the reference patient's displacement field map of exhale to inhale registration inside the voxel coordinates of the ROI of this patient.

The last step was putting all the interpolations into one model. The following graph shows the population mean histogram.

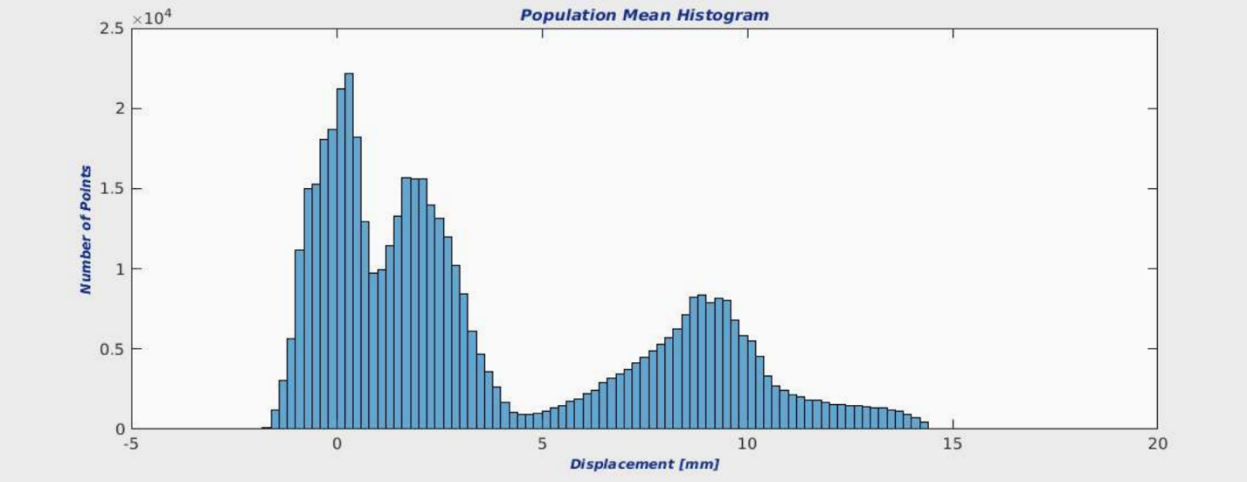

(Figure 3.3.15) Population Mean Histogram

From the above histogram, all the displacements are approximately between -1 mm and 14 mm. The major displacements are occurred to the positive direction (S/L/P). Graphing each axis separately, the x axis (left/right) direction of the displacement is shown below.

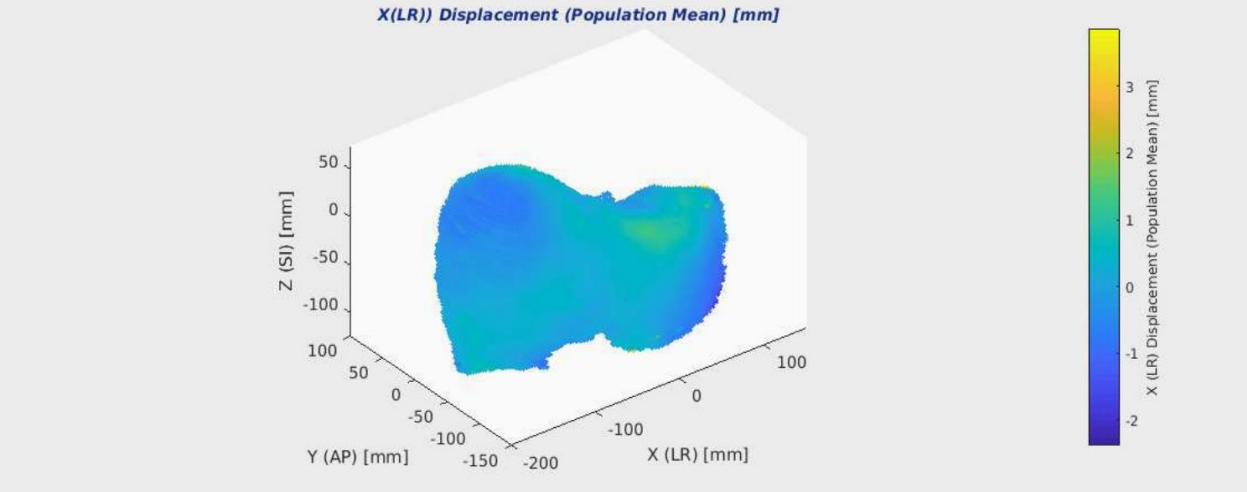

(Figure 3.3.16) X (LR) Displacement (Population Mean)

It can be observed from the above liver figure that the most displacement happened on the left direction. The following histogram is a supportive argument for our idea.

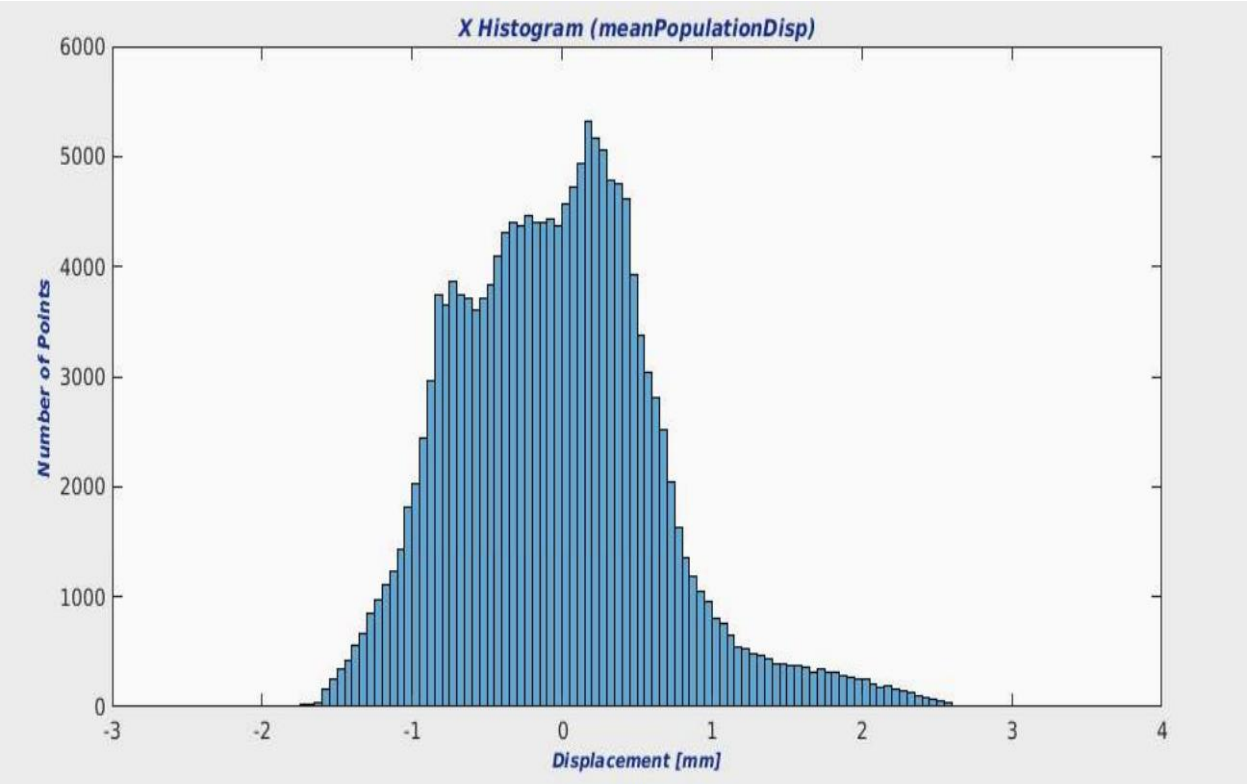

(Figure 3.3.17) Population Mean x Histogram

It can be observed that most of the displacement to the positive direction, which is the left direction.

The following figure shows the y displacement.

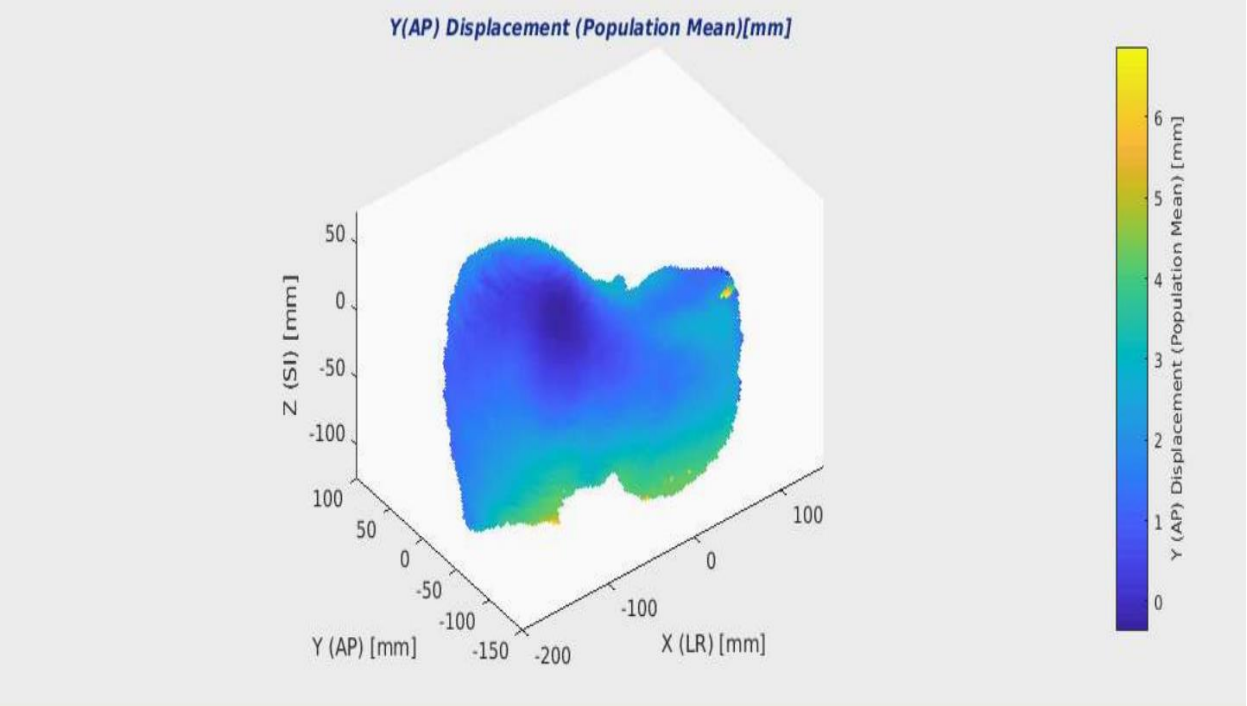

(Figure 3.3.18) Y (AP) Displacement (Population Mean)

From the above graph, the displacement is toward the posterior direction. The following histogram shows that most of the displacement is toward the positive direction.

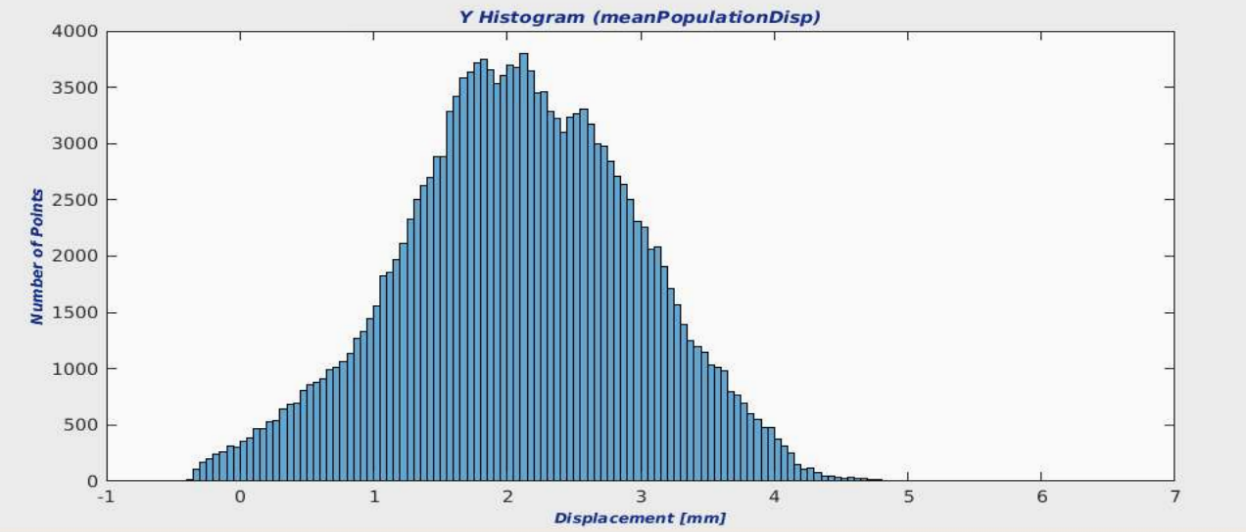

(Figure 3.3.19) Population Mean Y Histogram

For z axis (SI), the following figure shows that most of the displacement is toward the superior direction.

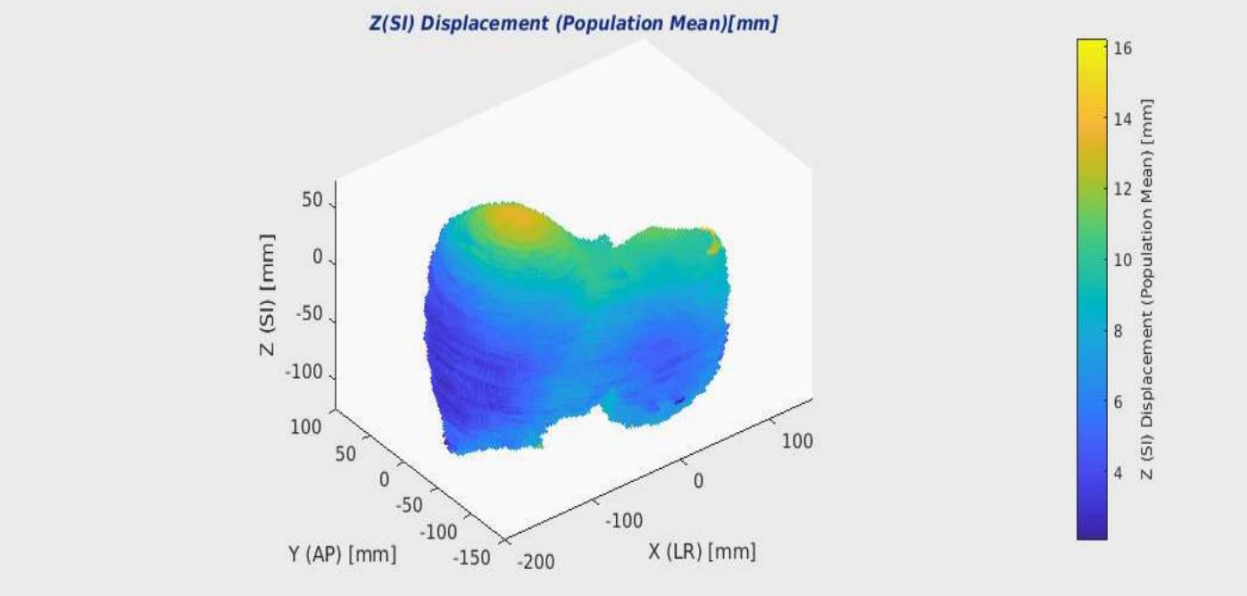

(Figure. 3.3.20) Z (SI) Displacement (Population Mean)

The following histogram shows that all the displacement is toward the positive direction, which is the superior direction.

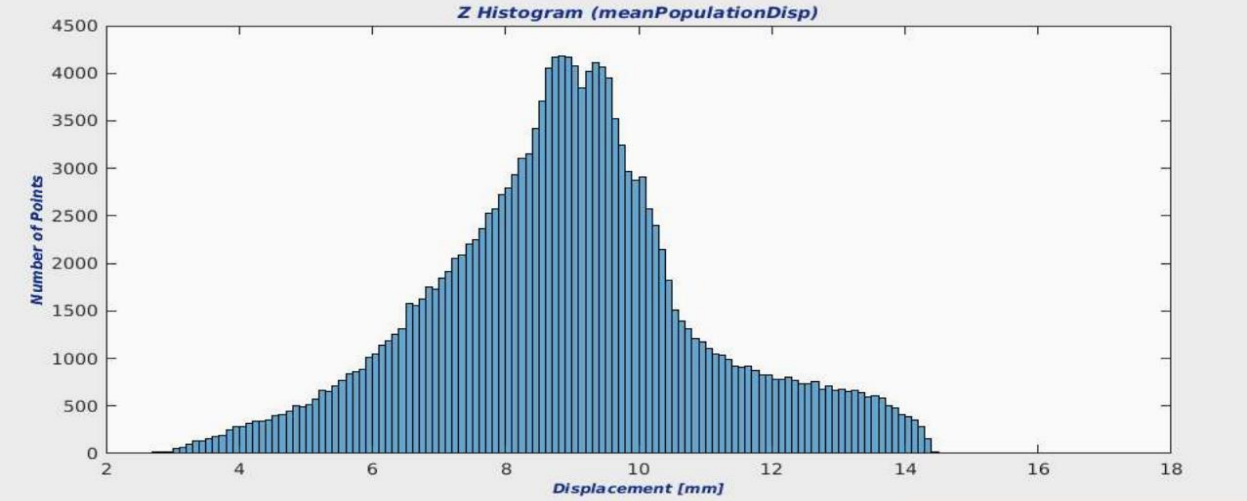

(Figure. 3.3.21) Population Mean Z Histogram

The following table shows a summary of the displacement toward LR, AP, and SI of the mean population liver model resulting from 30 liver patients

Coordinates	Mean [mm]	SD [mm]	Max [mm]	Min [mm]
X (Left, Right)	-0.03467	0.6785	3.8646	-2.3832
Y (Anterior, Posterior)	2.0907	0.8825	6.8692	-0.3661
Z (Superior, Inferior)	8.9314	2.0743	16.2344	2.0661

Table (3.3.2) Mean Displacement Fields of the Population Mean

From table (3.3.2), the highest displacement is toward SI direction. The overall displacement of the final liver model among a population is toward superior/right/posterior direction.

The following figure shows the mean and standard deviation of the mean population liver model.

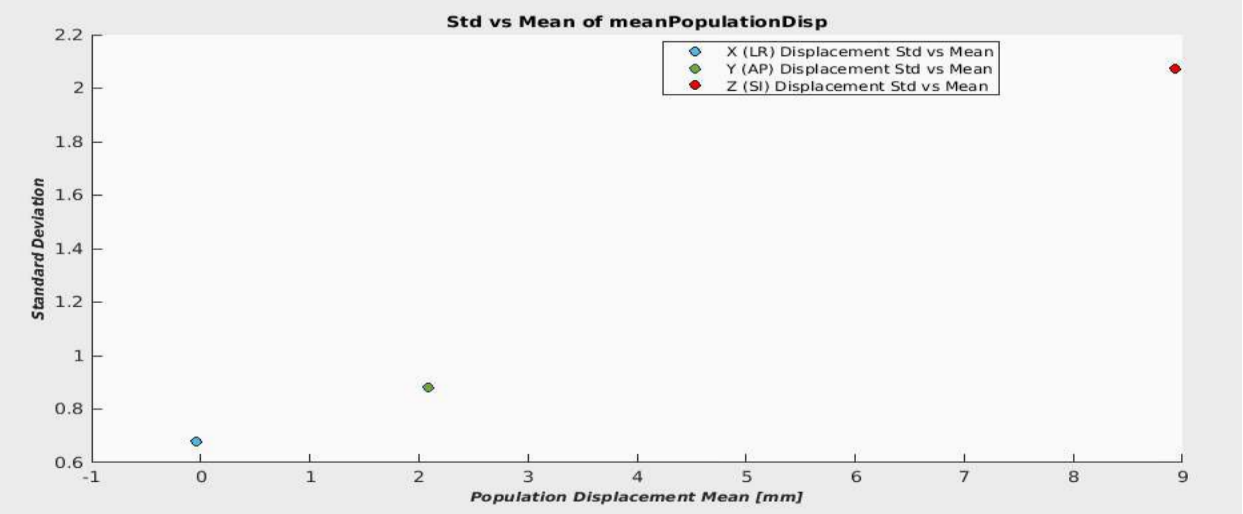

(Figure 3.3.22) Std vs Mean of the Mean Population Displacement

It can be observed from Figure 3.3.22 that the highest displacement is through the SI direction with high mean displacement and high standard deviation.

The following graph shows the x, y, z displacement for the mean population model.

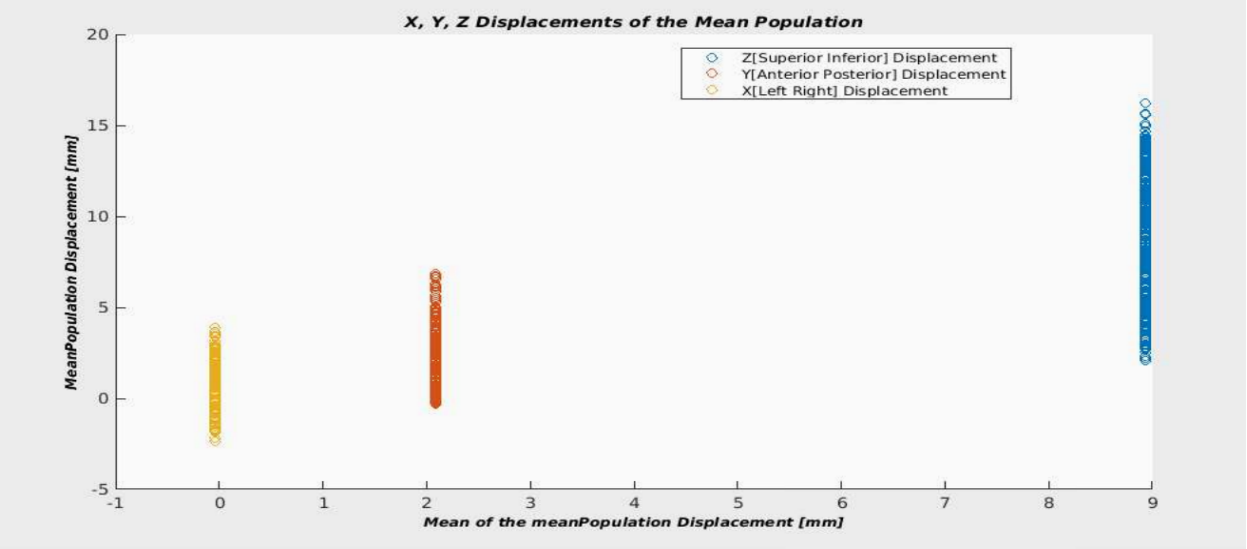

(Figure. 3.3.23) X, Y, Z Displacements of the Mean Population

From the above graph, the z displacement (SI) is the largest displacement.

3.4 Conclusion

A mean population displacement model was created. By following the preprocessing steps when drawing a manual liver ROI for each patient, we successfully deformed just the liver and avoid other parts of the image. Applying MORFEUS, thousands of deformed and un-deformed nodes were calculated. Then, the displacement field map of exhale to inhale of each patient was sampled to the MORFEUS un-deformed nodes for the related patient. After that, the new locations of the displacement field in the MORFEUS un-deformed nodes are assigned to the related deformed nodes. The final step is to apply a linear interpolation. This done by resampling the combination of the nodes-displacements into the voxel locations of the reference patient. The result is added to one model and this model is the mean population model of 30 liver patients.

CHAPTER 4

Conclusion and Future Work

To localize liver tumor position and destroy it, we need a high and a precise way to deliver the dose to the tumor. This will possible by align the treatment images with the planning images and make sure they match each other. Breathing motion of the liver is a really challenging task for delivering a precise dose to the target. Because the liver motion during breathing varies from day to day for one patient and for sure from one patient to other. This encouraged us to study the deformation of the liver during breathing among 30 patients. We modeled the start-phase of inhale to the end-phase of exhale for each patient and got the displacement fields map for them. After getting the displacement field, we conducted an analysis for this map and found out that the maximum displacement of the individual patient is toward superior/inferior direction and the minimum displacement is toward left/right direction. After that, we drew a manual ROI for each liver patient. Then, we applied MORFEUS to get a biomechanical model. We performed sampling of the reference patient displacement field to the MORFEUS un-deformed nodes and got the new locations of the nodes inside the reference patient displacement field. We took the liver ROI of the reference patient and extracted the individual voxel coordinates. Then, we interpolated linearly the combination of MORFEUS deformed nodes with the sampled displacement field to the reference voxel coordinates. All patients now are in the same 3D space. The last step was putting all the

resulted values in one model and then taking the average of these values. This mean of the population displacement is the final model. The resulted values represent the x, y, and z displacements of the mean population displacement model. The maximum displacement in this model is toward the SI direction with approximately 8.9314 ± 2.0743 mm.

BIBLIOGRAPHY

[1]. 1Ferlay J, Soerjomataram I, Ervik M, Dikshit R, Eser S, Mathers C et al. GLOBOCAN 2012 v1.0, Cancer Incidence and Mortality Worldwide: IARC CancerBase No. 11 Lyon, France: International Agency for Research on Cancer; 2013.

[2]. "Common Anatomy." *Interactive 3D Liver Anatomy*. University of Toronto, n.d. Web. 11 June 2017.

[3]. "Liver cancer." *Mayo Clinic*. Mayo Foundation for Medical Education and Research, 24 Mar. 2016. Web. 10 June 2017.

[4]. "Understanding Liver Cancer -- Diagnosis and Treatment." *WebMD*. WebMD, n.d. Web. 11 June 2017.

[5]. "What Is Liver Cancer?" American Cancer Society. N.p., 31 Mar. 2016. Web. 05 June 2017.

[6]. "Liver Cancer Survival Rates | Cancer of the Liver Survival Rates." American Cancer Society. N.p., 31 Mar. 2016. Web. 05 June 2017.

[7]. Types of Treatment - Surgery. American Cancer Society. (May-1-2008).

[8]. "Liver Cancer." Types of Surgery | Liver Cancer | Cancer Research UK. N.p., 28 Feb. 2015. Web. 05 June 2017.

[9]. "Liver Cancer Surgery." American Cancer Society. N.p., n.d. Web. 05 June 2017.

[10]. "Liver Cancer." About Chemotherapy | Liver Cancer | Cancer Research UK. N.p., 05 Feb. 2015. Web. 05 June 2017.

[11]. "Chemotherapy for Liver Cancer." American Cancer Society. N.p., n.d. Web. 05 June 2017.

[12]. T.A.Aloia, R.Adam, D.Samuel, D.Azoulay, and D.Castaing. "A Decision Analysis Model Identifies the Interval of Efficacy for Transarterial Chemoembolization 146 in Cirrhotic Patients with Hepatocellular Carcinoma Awaiting Liver Transplantation," 11[10]: 1328-1332 (2007).

[13]. "INTRODUCTION TO RADIATION THERAPY." SEER Training:Introduction to Radiation Therapy. National Cancer Institute, n.d. Web. 05 June 2017.

[14]. "Radiation Therapy for Cancer." National Cancer Institute. NIH National Cancer Institute, 30 June 2010. Web. 06 June 2017.

[15]. "Rising XR-29 Penalties Spur CT Dose Management Innovation." *Imaging Technology News*. N.p., 07 June 2017. Web. 10 June 2017.

[16]. "Liver cancer." *Mayo Clinic*. Mayo Foundation for Medical Education and Research, 24 Mar. 2016. Web. 10 June 2017.

[17]. Carter, Devon. "Radiation therapy: What it is and what to expect." *MD Anderson Cancer Center*. N.p., n.d. Web. 10 June 2017.

[18]. Radiation Therapy Principles. (2008).

[19]. "Tumor Ablation for Liver Cancer." Tumor Ablation for Liver Cancer. American Cancer Society, n.d. Web. 19 June 2017.

[20]. "Embolization Therapy for Liver Cancer." Embolization Therapy for Liver Cancer. American Cancer Society, n.d. Web. 19 June 2017.

[21]. "Targeted Therapy for Liver Cancer." Targeted Therapy for Liver Cancer. American Cancer Society, n.d. Web. 19 June 2017.

[22]. Radiation therapy and you: Support for people with cancer. National Cancer Institute. http://www.cancer.gov/cancertopics/radiation-therapy-and-you. Accessed Dec. 21, 2016.

[23]. Barbara Woodward Lips Patient Education Center. An introduction to radiation simulation and treatment. Rochester, Minn.: Mayo Foundation for Medical Education and Research; 2015.

[24]. Foote RL (expert opinion). Mayo Clinic, Rochester, Minn. Jan. 31, 2017.

[25]. Niu, Jiafei. Experimental Validation of Mathematical Models to Include Biomechanics into Dose Accumulation Calculation in Radiotherapy. Diss. 2009.

[26]. "CT Simulation for Radiation Therapy." Mount Sinai Medical Center. N.p., n.d. Web. 02 Aug. 2017.

[27]. Evans, P. M. "Anatomical Imaging for Radiotherapy," 53[12]: R151-R191

[28]. Report 50: Prescribing, Recording and Reporting Photon Beam Therapy. International

[29]. J.M.Calvin, G.Ezzel, A.Eisbrauch, C.Yu, B, Butler, Y.Xiao, I.Rosen, and J.Rosenman. "Implementing IMRT in Clinical Practice: A Joint Document of the American Society of Therapeutic Radiology and Oncology and the American Association of Physicists in Medicine," 58[5]: 1616-1634 (Apr-2004).

[30]. K.K.Brock, M.Hawkins, C.Eccles, J.L.Moseley, D.J.Moseley, D.A.Jaffray, and L.A.Dawson. "Improving Image-Guided Target Localization Through Deformable Registration,"(2008).

[31]. M.Bucci, A.Bevan, and M.Roach. "Advances in Radiation Therapy: Conventional to 3D, to IMRT, to 4D, and Beyond," 55[2]: 117-134 (2005).

[32]. K.M.Langen and D.T.Jones. "Organ Motion and Its Management," 50[1]: 265-278 (May-1-2001).

[33]. Y.Negoro, Y.Nagata, T.Aoki, T.Mizowaki, N.Araki, K.Takayama, M.Kokubo, S.Yano, S.Koga, K.Sasai, Y.Shibamoto, and M.Hiraoka. "The Effectiveness of an Immobilization Device in Conformal Radiotherapy for Lung Tumor: Reduction of Respiratory Tumor Movement and Evaluation of the Daily Setup Accuracy," 50[4]: 889-898 (2001).

[34]. Niu, Jiafei. “Experimental Validation of Mathematical Models to Include Biomechanics into Dose Accumulation Calculation in Radiotherapy.” 2009, pp. 11–12., tspace.library.utoronto.ca/bitstream/1807/18938/6/Niu_Jiafei_200911_MHSc_thesis.pdf.

[35] Tessa N. van de Lindt, Gerald Schubert, Uulke A. van der Heide, Jan-Jakob Sonke, An MRI-based mid-ventilation approach for radiotherapy of the liver, Radiotherapy and Oncology, Volume 121, Issue 2, 2016, Pages 276-280, ISSN 0167-8140, http://dx.doi.org/10.1016/j.radonc.2016.10.020.

[36]. H.D. Kubo, B.C. Hill Respiration gated radiotherapy treatment: a technical study Phys Med Biol, 83 (1996)

[37]. P.J. Keall, S. Joshi, S.S. Vedam, et al. Four-dimensional radiotherapy planning for DCML based respiratory motion tracking Med Phys, 942 (2005)

[38]. J.W.H. Wolthaus, J.J. Sonke, M. van Herk, et al. Comparison of different strategies to use four-dimensional computed tomography in treatment planning for lung cancer patients Int J Radiat Oncol Biol Phys, 70 (2008), pp. 1229-1238

[39]. Rueckert, D., L.i. Sonoda, C. Hayes, D.l.g. Hill, M.o. Leach, and D.j. Hawkes. "Nonrigid registration using free-form deformations: application to breast MR images." IEEE Transactions on Medical Imaging 18.8 (1999): 712-21. Web.

[40]. Marc Modat, Gerard R. Ridgway, Zeike A. Taylor, Manja Lehmann, Josephine Barnes, David J. Hawkes, Nick C. Fox, Sébastien Ourselin, Fast free-form deformation using graphics processing units, Computer Methods and Programs in Biomedicine, Volume 98, Issue 3, 2010, Pages 278-284, ISSN 0169-2607, http://dx.doi.org/10.1016/j.cmpb.2009.09.002.

[41]. 20K. K. Brock, M. B. Sharpe, L. A. Dawson, S. M. Kim, and D. A. Jaffray, "Accuracy of finite element model (FEM)-based multi-organ deformable image registration," Med. Phys. 326, 1647–1659 (2005).

[42]. Nguyen, T.-N., Moseley, J. L., Dawson, L. A., Jaffray, D. A. and Brock, K. K. (2009), Adapting liver motion models using a navigator channel technique. Med. Phys., 36: 1061–1073. doi:10.1118/1.3077923

[43] Fatma El-Zahraa Ahmed El-Gamal, Mohammed Elmogy, Ahmed Atwan, Current trends in medical image registration and fusion, Egyptian Informatics Journal, Volume 17, Issue 1, 2016, Pages 99-124, ISSN 1110-8665, http://dx.doi.org/10.1016/j.eij.2015.09.002.

[44] Hajnal J, Hawkes D, Hill D. Medical image registration. Boca Raton: CRC Press; 2001.

[45] Khalifa F, Beache G, Gimel'farb G, Suri J, El-Baz A. State-ofthe- art medical image registration methodologies: a survey. In: Multi-modality state-of-the-art medical image segmentation and registration methodologies; 2011. p. 235–80.

[46] Duy L. Review and enhancement optimization methods in image registration. MEng. Computing, Department of Computing, Imperial College London; 2009.

[47] Mani V, Arivazhagan D. Survey of medical image registration. J Biomed Eng Technol 2013;1(2):8–25.

[48] ALBERTINI, SILVIA, and FRANCESCA IUDICELLO. "Global respiratory motion model based on 4D CT and 2D cine-MRI." (2016).

[49] Shackleford J.A., Kandasamy N., Sharp G.C, On developing B-spline registration algorithms for multi-core processors, Physics in Medicine and Biology, Vol 55, No 21, pp 6329-6351, Nov 7, 2010.